Application of Nano-Scale Geomechanics Using PeakForce Quantitative Nano-Mechanical Mapping to Improve Hydraulic Fracture Design in Highly Heterogeneous Reservoirs

©2020

Kim Sarah Mews

B.Sc. Geosciences, Kiel University, 2017

Submitted to the graduate degree program in Chemical and Petroleum Engineering and the Graduate Faculty of the University of Kansas in partial fulfillment of the requirements for the degree of Master of Science in Petroleum Engineering.

<table>
<tr><td></td><td>Dr. Reza Barati, Chair</td></tr>
<tr><td>Committee members</td><td>Dr. Anil Misra</td></tr>
<tr><td></td><td>Dr. Jyun-Syung Tsau</td></tr>
</table>

Date defended: August 21, 2020

The Thesis Committee for Kim Sarah Mews certifies
that this is the approved version of the following thesis :

Application of Nano-Scale Geomechanics Using PeakForce Quantitative Nano-Mechanical
Mapping to Improve Hydraulic Fracture Design in Highly Heterogeneous Reservoirs

_____

Dr. Reza Barati, Chair

Date approved: _____August 21, 2020_____

Abstract

The production of hydrocarbons from unconventional reservoirs is nowadays essential to meet the rising the demand for energy in the world. Unconventional reservoirs have a low porosity and an extremely low permeability, which requires horizontal drilling and multi-stage hydraulic fracturing. As hydraulic fracturing strongly depends on the principal stresses, the identification of geomechanical properties is key for the assessment of effective hydraulic fracturing design.

The assessment of geomechanical properties through macro-scale testing such as true triaxial testing has been performed for decades. However, heterogeneities on a nano-scale in addition to the possibility of having non-intact samples lead to the application of nano-scale geomechanical testing. PeakForce Quantitative Nano-mechanical mapping in atomic force microscopy (AFM PF-QNM) maps the geomechanical properties on a nano-scale requiring a sample size that is as small as drill cuttings. The testing reveal s the 3D heterogeneities within the sample indicating spots of highest and weakest strength. This way the anisotropy of the tested material can be assessed. However, only few studies with application of AFM PF-QNM on reservoir rocks have been performed.

Therefore, AFM PF-QNM testing has been performed and compared to the results from performed true triaxial testing for the Eagle Ford Formation. The results show a multi-scale comparison of geomechanical properties. As AFM PF-QNM testing assumes a preset value of Poisson's ratio, an iterative model that solves for Poisson's ratio in dependency of Young's modulus has been developed for the Eagle Ford Formation, as these properties are strongly lithology dependent. The new model corrects the Young's modulus in dependency of the Poisson's ratio. The results from AFM PF-QNM indicate many hundred thousand measurements. In order to reduce the large data set, exploratory factor analysis has been deployed. It determines if unmeasured factors could explain

the variance from the data set, which is caused by different minerals, macerals, textures, or pores. It shows that 34% of the data set can be explained by 6 factors. These different factors represent groups that are ductile, intergranular or of high strength.

The comparison with the results from true triaxial testing on a macro-scale indicate that AFM PF-QNM could yield similar results. True triaxial testing reveals the macro-scale anisotropy indicating a decreased velocity in Z-direction.

The results show that different testing methods performed at different spatial scales and different loading conditions, lead to different results. The dynamic Young's modulus from true triaxial testing indicates the highest value (69.7 GPa) and the static Young's modulus from true triaxial testing yields to the lowest value (42.6 GPa). The results from AFM PF-QNM show an average modulus (52.28 GPa) in between the static and dynamic results from true triaxial testing.

This thesis demonstrates a multi-scale geomechanical comparison for unconventional reservoirs. It improves the evaluation for AFM PF-QNM testing by correcting the Young's modulus iteratively in dependency of the Poisson's ratio. It reveals the advantages of AFM PF-QNM as it can be performed on samples that are as small as drill-cuttings determining the 3D heterogeneity of the material.

Acknowledgements

Finally, but most importantly, I would like to thank my mother, Ines Mews for her unconditional love and support. She taught me the value of dreams and hard work. Her faith and perseverance made this work possible. Danke, Mami.

Contents

List of Figures

List of Tables

Chapter 1

Introduction

Abstract

This chapter presents the motivation and the scope of the thesis. It is subdivided into distinct parts: the experimental realization of nano- and macro-scale testing, the theoretical work for evaluating AFM PF-QNM testing and the multi-scale comparison between the testing devices with application on the Eagle Ford Formation.

1.1 Motivation

The assessment of geomechanical properties in unconventional reservoirs is key in the simulation process of hydraulic fracturing treatments. Macro-scale geomechanical simulations often fail, because the reservoir heterogeneity has not been properly assessed. Geomechanical testing on a macro-scale, such as true triaxial testing, has been performed for decades. However, the drilling process and the brittle nature of the material complicate the sampling. Thus, the possibility of having non-intact samples and heterogeneities on a macro-scale, provides opportunities for nano-mechanical testing. PeakForce Quantitative Nano-mechanical mapping in atomic force microscopy (AFM PF-QNM) allows for mapping of elastic properties on a nano-scale.

AFM PF-QNM is a novel technique to measure the geomechanical properties on a nano-scale on samples that are as small as drill-cuttings. The first application of this technique has been accomplished by Eliyahu et al. (2015) on shale samples. Further studies focused on the elastic

1

properties of organic matter (Yang et al., 2017; Chen et al., 2017; Li et al., 2018; Eichmann et al., 2018; Li et al., 2018). As the procedure of AFM PF-QNM deviates strongly from conventional geomechanical testing methods, a comparison between macro-scale geomechanical testing methods and AFM PF-QNM is required.

AFM PF-QNM allows qualitative distinction of materials with different elastic properties. It results in the topographic imaging on each spot. However, this technique sets the Poisson's ratio, which is a measure of the amount of transverse strain divided by longitudinal strain, at a preset value. The Poisson's ratio is an important elastic property that is required for hydraulic fracturing design. It depends on the Young's modulus in dependency of the lithology. Thus, the development of a lithology dependent iterative model can solve for Young's modulus and Poisson's ratio at the same time.

There have been attempts for the interpretation of AFM PF-QNM results based on the strength of a material in phases that are rather ductile or brittle (Eliyahu et al., 2015). The results can be interpreted using a multivariate statistical tool: exploratory factor analysis (EFA). This method reduces a large set of variables into a much smaller set of factors. These unmeasured factors could help explain the relationships between diverse measurements resulting from different minerals. It could be caused by different minerals, macerals, textures, or pores. This method represents a novel technique to improve the interpretation of AFM PF-QNM results.

True trixial testing has been performed to compare the results from a macro-scale to tests on a nano-scale to determine if AFM PF-QNM could yield similar results as true triaxial testing. Differentiation between static and dynamic Young's modulus should be taken in account.

The motivation for this study is to raise awareness about micro- to nano-scale heterogeneity and their impact on mechanical properties by AFM PF-QNM. Micro- to nano-scale heterogeneity

would lead to more complex and heterogeneous fractures.

1.2 Objectives and Scope

The objective of this thesis is to introduce the novel technique AFM PF-QNM with application on one of the prolific, highly heterogeneous Eagle Ford (EF) formation to achieve a multi-scale geomechanical comparison.

The accomplishments of this work can be decomposed into the following distinct parts:

1. Experimental macro-scale testing has been realized performing true triaxial testing.

2. Experimental nano-scale testing has been realized performing AFM PF-QNM.

3. A theoretical iterative model for AFM PF-QNM that solves for Poisson's ratio in dependency of Young's modulus has been developed.

4. The AFM PF-QNM results has been statistically evaluated using exploratory factor analysis to reduce a large set of variables to a much smaller set of factors.

5. Macro-scale and nano-scale geomechanical testing has been compared.

Figure 1.1 shows a schematic of the scope of the thesis. It is divided into experimental and theoretical work. For the experimental work true triaxial testing and AFM PF-QNM has been performed. For the theoretical work, an iterative model in MATLAB® has been developed and EFA in RStudio® has been applied. The theoretical work is implemented to evaluate the AFM PF-QNM experimental data. The objective is to achieve a comparison between macro- and nano-scale geomechanical properties and to differentiate their applicability in terms of both scale and heterogeneity.

```
                    ┌─────────┐
              ┌─────│  Scope  │─────┐
              │     └─────────┘     │
              ▼                     ▼
    ┌──────────────────┐  ┌──────────────────┐
    │   Experimental   │  │   Theoretical    │
    │      Work        │  │      Work        │──┐
    └──────────────────┘  └──────────────────┘  │
        │        │                  │           │
        ▼        ▼                  ▼           │
   ┌────────┐┌────────┐   ┌──────────────────┐  │
   │  True  ││  AFM   │◄──│  Iterative Model │  │
   │ Triaxial││  PF-  │   └──────────────────┘  │
   │ Testing││  QNM   │◄──┌──────────────────┐  │
   └────────┘└────────┘   │       EFA        │◄─┘
        │        │        └──────────────────┘
        ▼        ▼
   ┌────────────────────────────────────────┐
   │  Comparison of Macro- and Nano-scale   │
   │       Geomechanical Properties         │
   └────────────────────────────────────────┘
```
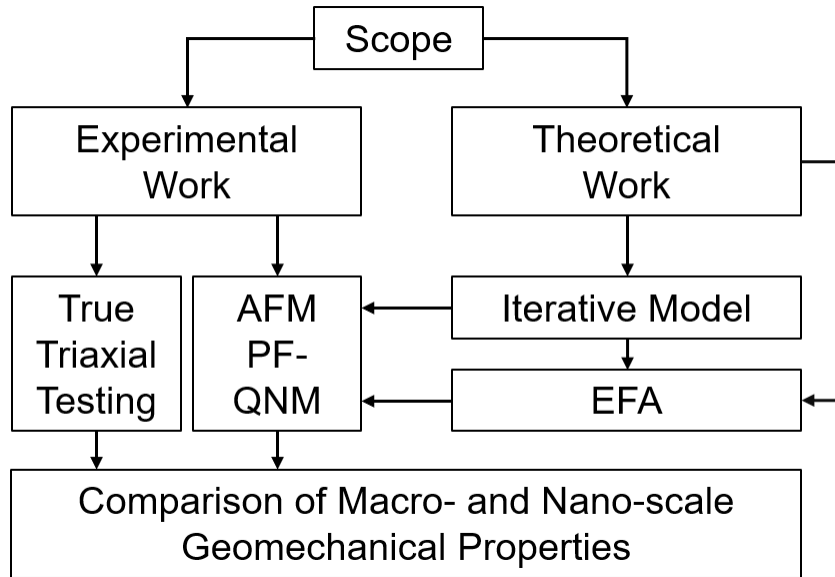
Figure 1.1: Schematics of the scope of the thesis divided into experimental and theoretical work.

1.3   Thesis Outline

Chapter 1 is an introduction on the motivation and the scope of this thesis to achieve a multi-scale geomechanical comparison. AFM PF-QNM has been applied to determine nano-geomechanical properties, whereas true triaxial testing has been utilized for the determination of macro-mechanical properties. An iterative model and a statistical method have been applied to improve the evaluation of AFM PF-QNM.

Chapter 2 encompasses a summary of existing Brittleness Index (BI) correlations derived from the mineralogy or from the elastic properties. A geomechanical characterization of unconventional reservoirs further explains in more detail geomechanical testing on different scales. A lithologic overview is given for the tested formation: the EF formation.

Chapter 3 focuses on the experimental procedures. XRD analysis and optical microscopical analysis have been performed to quantify the components of the tested material. The sample preparation, principle, device and steps and theoretical background of AFM PF-QNM are explained. The work

flow of the iterative model that solves for Poisson's ratio in dependency of Young's modulus is explained. Statistical methods that are used to reduce a large set of variables to a smaller set of factors is described. Further, the methodology and theory for true triaxial testing are explained. The theoretical model for AFM PF-QNM and true triaxial testing shows the differences between these methods on spatial scales.

Chapter 4 shows the results from AFM PF-QNM. Maps show the distribution of Young's modulus and indicate the strength and component's phases of each tested spot. The iterative model determining the Poisson's ratio as a function of Young's modulus has been applied. The reevaluated data is applied to the statistical evaluation. Exploratory factor analysis is applied to reduce the large data set by a smaller number of factors explaining the variance of the data. Further, the results from true triaxial testing are presented. Dynamic and static results along with the anisotropic behavior of the sample are analyzed. A connection between geomechanical testing on a nano-scale and a macro-scale has been achieved.

Chapter 5 is a summary of the most significant concluding remarks for geomechanical testing from this study on multiple scale for the Eagle Ford formation. Ideas for future works are explained.

Chapter 2

Literature Review

Abstract

This chapter presents the literature review. It starts with a review of brittleness index (BI) correlations, which play an important role in the evaluation of unconventional reservoirs. These reservoirs are geomechanically characterized and approaches approaches to derive elastic properties on different scales are explained. A literature review of Young's modulus values from different rock components and different prolific US plays will help explain the results from geomechanical testing. Next, the geological background of the Eagle Ford formation is presented. The last section reviews the definition of an overall brittleness index, but also a multi-scale comparison of geomechanical properties will lead to a more accurate prediction of elastic properties for unconventional reservoirs.

2.1 Brittleness Index Correlations

Brittleness is considered a key parameter in the evaluation of unconventional reservoirs for the design of hydraulic fractures. Brittle formations are more prone to hydraulic stimulation than ductile formations. The parameter brittleness is defined in many different ways from geomechanical testing results, but also from well logging information.

The BI indicates whether a formation is rather brittle, resulting in high values of BI and forming a large network of fractures (Grieser and Bray, 2007) or rather ductile resulting in low values

6

of BI, whereas all values are normalized to a scale between 0 and 1. The BI can be either derived from the geomechanical properties or from the mineralogy (Jarvie et al., 2007; Rickman et al., 2008; Wang and Gale, 2009; Buller et al., 2010; Glorioso and Rattia, 2012; Sharma and Chopra, 2012; Sun et al., 2013; Chen et al., 2014; Jin et al., 2014; Alzahabi et al., 2015; Rybacki et al., 2015; Mews et al., 2019).

It describes the rock failure of a material (Kivi et al., 2018) and is a function of mineral composition, total organic carbon (TOC), in-situ temperature, diagenesis, effective stress, porosity, type of fluid and the overall lithology (Wang and Gale, 2009). An extensive review has shown that the BI is a complex function of lithology and that it can be divided into formations that are either dominated by silicates, carbonates, clay or a strongly heterogeneous mineralogy (Mews et al., 2019). Mews et al. (2019) evaluated distinct formations with varying mineralogy, showing that an ideal candidate for hydraulic fracturing consists of a high silica or carbonate content (Mews et al., 2019).

2.2 Geomechanical Characterization of Unconventional Reservoirs

The U.S. Energy Information Administration (EIA) states that most wells drilled in the US in 2016 (69%) were hydraulic fractured (Cook et al., 2018). Also, an increase of 17% in crude oil production is attributed with formations that were horizontally drilled and hydraulic fractured, as the rocks were too tight for conventional production (Geary, 2019). Therefore, a qualitative geomechanical analysis will increase the accuracy of hydraulic fracturing design and the production from unconventional reservoirs.

There are different ways to derive the geomechanical properties such as Young's modulus and Poisson's ratio. Studies have shown that a high Young's modulus and a low Poisson's ratio indicate a high BI and therefore a high probability to generate hydraulic fractures (Ghanizadeh et al.,

2015). On a macro-scale the geomechanical properties are derived from well logs. Dipole sonic

logging measures the seismic velocities with a resolution of 60 cm (Mazaheri et al., 2015) and a

depth of investigation of 15 cm (Bond et al., 2010) along the entire formation. On a meso-scale

the geomechanical properties are derived from rock samples. For true triaxial testing of this study

a sample size of 4 cm^3 is required. Testing devices commonly used besides true triaxial testing

are indirect tensile strength using Brazilian loading, multi-compression tests, triaxial compression

tests, unconfined compressive strength tests and ultrasonic velocity measurements. On a nano-

scale the geomechanical properties are derived from AFM PF-QNM, where only drill-cutting-size

samples are required. Figure 2.1 shows an overview of ways to derive the elastic properties on

multiple scales.
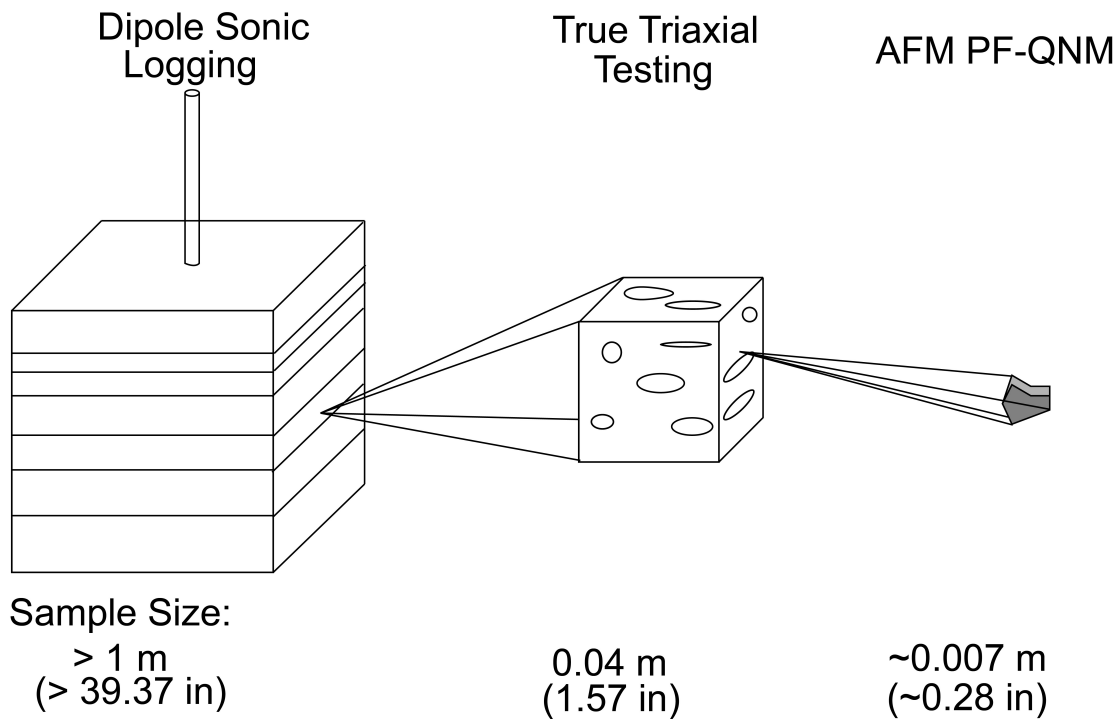
Figure 2.1: Approaches to derive the elastic properties on a macro-scale (left) derived from dipole sonic logging, on a meso-scale (center) derived from true triaxial testing and on a nano-scale (right) derived from PeakForce Quantitative Nanomechanical mapping. For dipole sonic logging, there is no specific required sample size, as the properties are measured in-situ. For true triaxial testing a sample size of 4 cm^3 is required and for AFM PF-QNM drill-cutting-size samples in the order of 7 mm are sufficient for geomechanical testing.

8

The results from dipole sonic logging represent the value over the entire depth of investigation. The results from true triaxial testing show the averaged value over the entire size of the sample. It has been shown that the behavior of rocks depends on the particles (size and shape), their contacts and interaction occurring during the loading, the properties of the surface and the change during the loading (Poorsolhjouy and Misra, 2017). However, heterogeneity and anisotropy do exist on a much smaller scale, and anisotropy does not follow trends on a large scale (Li and Sakhaee-Pour, 2016). These parameters can be detected on a nano-scale using AFM PF-QNM. Another advantage of this technique is the small sample size. The sampling for geomechanical testing on a macro-scale bears challenges, as the rocks are exposed to additional stress trough the drilling process. This stress can induce cracks that will change the elastic properties resulting in the closure of the cracks at low confining stresses and thus an underestimation of the material strength. Furthermore, the brittle nature of the rocks complicated the sampling process so that it is hard to find an intact sample of the required geomechanical testing size.

AFM PF-QNM is a novel partially destructive technique, that maps the mechanical properties of the surface in high-speed revealing complex structures on a nano-scale (Li et al., 2018). Dipole sonic logging and true triaxial testing measure the seismic velocities, whereas this technique depends on the mechanical interaction between the surface of the sample and an oscillating tip. Several studies on organic matter and shales using AFM PF-QNM have been performed so far (Eliyahu et al., 2015; Liu et al., 2016; Yang et al., 2017; Chen et al., 2017; Li et al., 2018). The results reveal heterogeneities among the sample.

In order to interpret the results from AFM PF-QNM, the knowledge of the Young's modulus for the single rock components is important. Table 2.1 shows the Young's modulus for different rock components from the literature. It shows that quartz and calcite reveal high values of Young's modulus indicating brittle behavior. Organic matter shows very low values of Young's modulus resulting in ductile behavior. Eliyahu et al. (2015) grouped the Young's moduli results from AFM

Table 2.1: Literature values of Young's modulus for different rock components.

Component	Young's Modulus (GPa)	Reference
Quartz	90-100	Simmons and Wang (1971)
Quartz	50-70	Wilkinson et al. (2015)
Calcite	69-98	Simmons and Wang (1971)
Clays	15-45	Wilkinson et al. (2015)
Softer intergranular phase	0-25	Eliyahu et al. (2015)
Intergranular matrix	28-30	Eliyahu et al. (2015)
Isolated grains	49-67	Eliyahu et al. (2015)
Stiff mineral phase	>90	Eliyahu et al. (2015)
Kerogen	10	Wilkinson et al. (2015)
Organic matter	<20	Eichmann et al. (2018)
Organic matter	3-12	Li et al. (2018)
Organic matter	7-23	Li et al. (2018)

PF-QNM into a softer intergranular phase, intergranular matrix, isolated grains and a stiff mineral phase.

Previous results for Young's modulus from geomechanical testing on samples from the entire formation, instead of single components, is summarized in table 2.2. It shows nanoindentation and triaxial testing studies from the literature for the Eagle Ford, Wolfcamp, Barnett, Middle and Lower Bakken, Haynesville and Niobrara formation. These formations are dominated by different mineralogy, contain a different content of organic matter, and contain a different texture and pore space distribution, which leads to different results for Young's modulus.

The Eagle Ford formation is described in more detail in the geological background (chapter 2.3). The results from previous studies on this formation indicate a static Young's modulus of 30 to 52 GPa determined from nanoindentation measurements and a static Young's modulus of 21 to 39 GPa for measurements from triaxial testing.

The Wolfcamp formation is highly heterogeneous. It is subdivided into Wolfcamp A, B, C and D, whereas A is the mostly the producing horizons. Wolfcamp A consists of interbedded carbonate-

Table 2.2: Average Young's moduli derived for different unconventional plays in the US through either AFM PF-QNM, nanoindentation or triaxial testing. The results from triaxial testing indicate, whether it is the static or the dynamic Young's modulus. Nanoindentation is another technique to determine the geomechanical properties on a nano-scale and will be explained in more detail in chapter 3.4.5.

Formation	Nanoindentation	Triaxial Testing	Reference
Eagle Ford	30-52 GPa		Shukla (2013)
		21-39 GPa (static)	Hu et al. (2014)
		26 GPa (static)	Ye et al. (2018)
		23-35 GPa (static)	Mokhtari et al. (2016)
	35-45 GPa		Akrad et al. (2011)
Wolfcamp	26-31 GPa		Shukla et al. (2013)
	43-51 GPa		Shukla (2013)
Barnett	38-73 GPa		Shukla et al. (2013)
	46-74 GPa		Akrad et al. (2011)
	44-56 GPa		Shukla (2013)
	33-50 GPa	46 GPa (dynamic)	Shukla et al. (2014)
Middle Bakken	57-74 GPa		Akrad et al. (2011)
Lower Bakken	24-47 GPa		Akrad et al. (2011)
Haynesville	39 GPa		Akrad et al. (2011)
	31-63 GPa		Shukla (2013)
Niobrara	38-53 GPa		Corapcioglu et al. (2014)

and siliciclastic-rich strata (Flotron et al., 2019) with an overall TOC of 0.23-6.35% (Hackley et al., 2020). Gupta et al. (2017) use principal component analysis on the Wolfcamp formation for results derived through well logging measurements resulting in three types of classification: type 1 with the highest porosity and highest TOC, type 2 with intermediate porosity and TOC and type 3 with the highest carbonate content. The Young's modulus from this study is between 30 to 80 GPa (Gupta et al., 2017).

The Barnett formation is rich in quartz, carbonate and clay (Kumar et al., 2012). The results reveal Young's moduli ranging from 33 GPa (Shukla et al., 2014) to 74 GPa (Akrad et al., 2011), indicating that this formation is highly heterogeneous as well.

The Bakken formation consists of the Upper, Middle and Lower Bakken, whereas the Upper and

the Lower Member can be described as organic-rich shales, which are the source beds (Pu, 2013). The Middle Bakken is the primary target for hydraulic fracturing due to its higher permeability (Pu, 2013). It consists of dolomitic siltstone or silty dolostone and sandstone with a low TOC (Pu, 2013). The results from nanoindentation confirm that the Middle Bakken is more brittle with higher results for Young's modulus, whereas the Lower Bakken reveals low values of Young's modulus (Akrad et al., 2011). It is worth to mention that the results from Akrad et al. (2011) were taken from the average of 25 nanoindentation measurements.

The Haynesville formation has clay and carbonate as dominant minerals (Kumar et al., 2012) indicated by a wide range of Young's moduli results from nanoindentation studies from Shukla et al. (2013).

The Niobrara formation consists of four chalk units with three intervening marl intervals (Cho et al., 2016). The Young's modulus is in the range of 38 GPa to 53 GPa based on nanoindentation measurements (Corapcioglu et al., 2014).

The comparison of Young's moduli results from geomechanical testing for different formations and the wide distribution of Young's moduli results indicate the necessity for nano-mechanical testing that reveals the weakest and the strongest moduli of the rock sample.

2.3   Geologic Background

It has been shown that the geomechanical properties strongly depend on the lithology (Mews et al., 2019). For this study a prolific unconventional plays located in Texas has been chosen: the Eagle Ford formation.

The mineralogical composition of Eagle Ford formation varies areal and vertically strongly (Mokhtari

et al., 2016). It is a low-porosity reservoir with values ranging from 2% to 9% and a TOC content varying between 2.10% and 6.86% (Li, 2017). The mineralogy shows a dominant carbonate fraction from carbonate mudstone with stringers consisting of dense calcite (Li, 2017). The clay content is highly heterogeneous and varies from 2% (Jansen, 2014) to 51% (Ergene, 2014). Even though the clay content can be extremely high, the formation is due to its high carbonate content an ideal candidate for hydraulic fracturing leading to high values of BI.

Chapter 3

Material and Methods

Abstract

This chapter explains the material and the methods. XRD analysis and microscopical analysis, which were performed to characterize the material, are introduced. In order obtain the nano-mechanical properties, AFM PF-QNM testing has been performed. The preparation of the sample, the principle, device and steps, and the theoretical model are explained. AFM PF-QNM testing is compared to nanoindentation, another instrument to obtain the geomechanical properties on a nano scale. The surface roughness evaluation and the influence of the area below the surface are pointed out. The iterative model to solve for Poisson's ratio in dependency of Young' modulus is introduced. Boundary conditions reveal the quality of the data. Further, statistical methods such as analysis of variance and exploratory factor analysis are demonstrated to evaluate the large dataset of results from AFM PF-QNM. In order to obtain the geomechanical properties on a macro-scale, true triaxial testing has been performed. The preparation of the sample, the principle, device and steps, and the theory behind the testing are explained. The background information for geomechanical testing on a nano-scale and for geomechanical testing on a macro-scale will help to draw a connection between these methods and the interpretation of the results.

3.1 Sample Material

Two samples that reveal a similar mineralogy have been chosen, one from a reservoir and one from an outcrop. True triaxial testing has been performed on the reservoir sample and AFM PF-QNM on the outcrop sample. The analysis has been performed on different samples, as the required sample size for true triaxial testing was not accessible. Figure 3.1 shows the prepared sample for AFM PF-QNM (Figure 3.1a) and for true triaxial testing (Figure 3.1b), respectively. They differ in size as the sample for AFM PF-QNM has drill-cutting-size and the true triaxial testing requires a 4 cm cube. It was found that the Young's modulus is lower normal to bedding than along bedding (Wang et al., 2018). This is important to consider that AFM PF-QNM testing has been applied along the bedding, whereas true triaxial testing is measured along the bedding (X-direction and Y-direction) and normal to the bedding (Z-direction).

The optical analysis of the true triaxial testing sample reveals fine lamination. As the tensile strength along laminations is lower, the velocity in Z-direction is decreased (Mokhtari et al., 2014a). Studies on the Eagle Ford Formation revealed foraminifera-rich lamina with pores filled with kaolinite or calcite and associated with pyrite (Mokhtari et al., 2014b). This results in a higher density and higher wave velocities (Mokhtari et al., 2014b). An increased calcite content results in a weak anisotropic behavior(Mokhtari et al., 2016), which will be examined in the true triaxial testing.

Figure 3.2 shows the well log for the reservoir sample. The green line shows the Gamma Ray values. A high gamma ray value corresponds to a high clay content (Jin et al., 2014).

3.2 XRD Analysis

X-Ray Diffraction (XRD) is a destructive technique to characterize crystalline materials (Kohli and Mittal, 2012). Therefore, the detection of clay minerals is difficult, when they only present in small weight percentages. Furthermore, kerogen is x-ray amorphous. Based on the petrographic
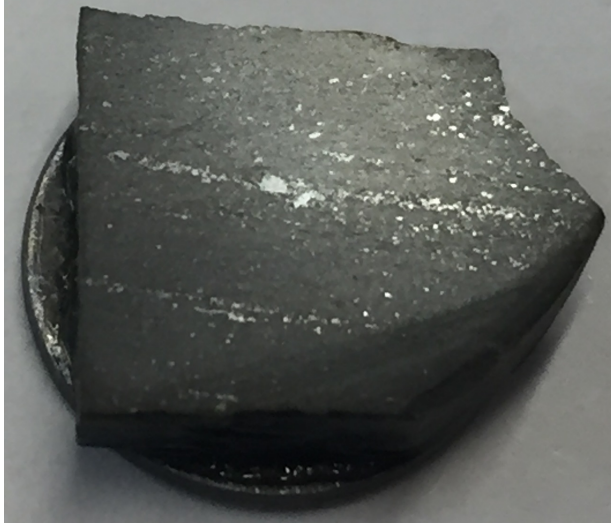
(a) Sample prepared for AFM PF-QNM   (b) Sample prepared for true triaxial testing
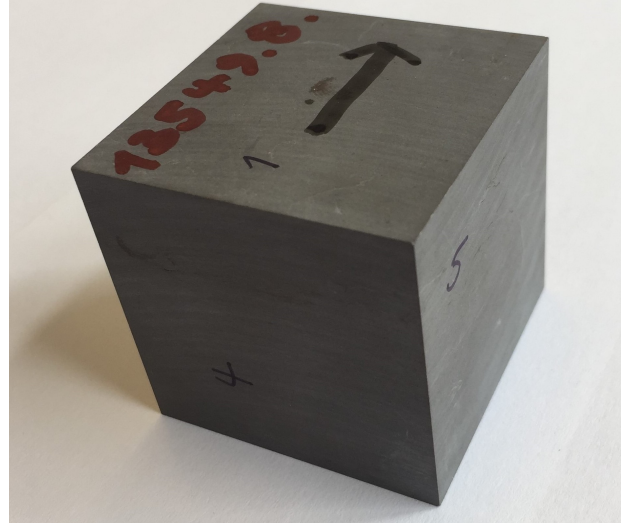
Figure 3.1: The photos show the prepared samples for AFM PF-QNM (left) and true triaxial testing (right). The AFM PF-QNM sample (3.1a) has a size of approximately 9 x 8 x 3 mm (l x w x h). The true triaxial sample shows a 4 cm cube.

analysis it is expected that the samples contain both, organic particles and clay minerals, which would not show in the XRD analysis.

3.3 Microscopical Analysis

Optical microscopy of thin sections has been performed on the sample from AFM PF-QNM testing and from true triaxial testing, respectively. The establishment of the thin sections is destructive and therefore has been performed after the testing of samples has been accomplished. The microscopical analysis allows for the characterization of the internal structure and non-crystalline materials, which cannot be detected with XRD analysis. Transmitted light optical microscopy was performed on the thin sections with crossed and plane-polarized polars.
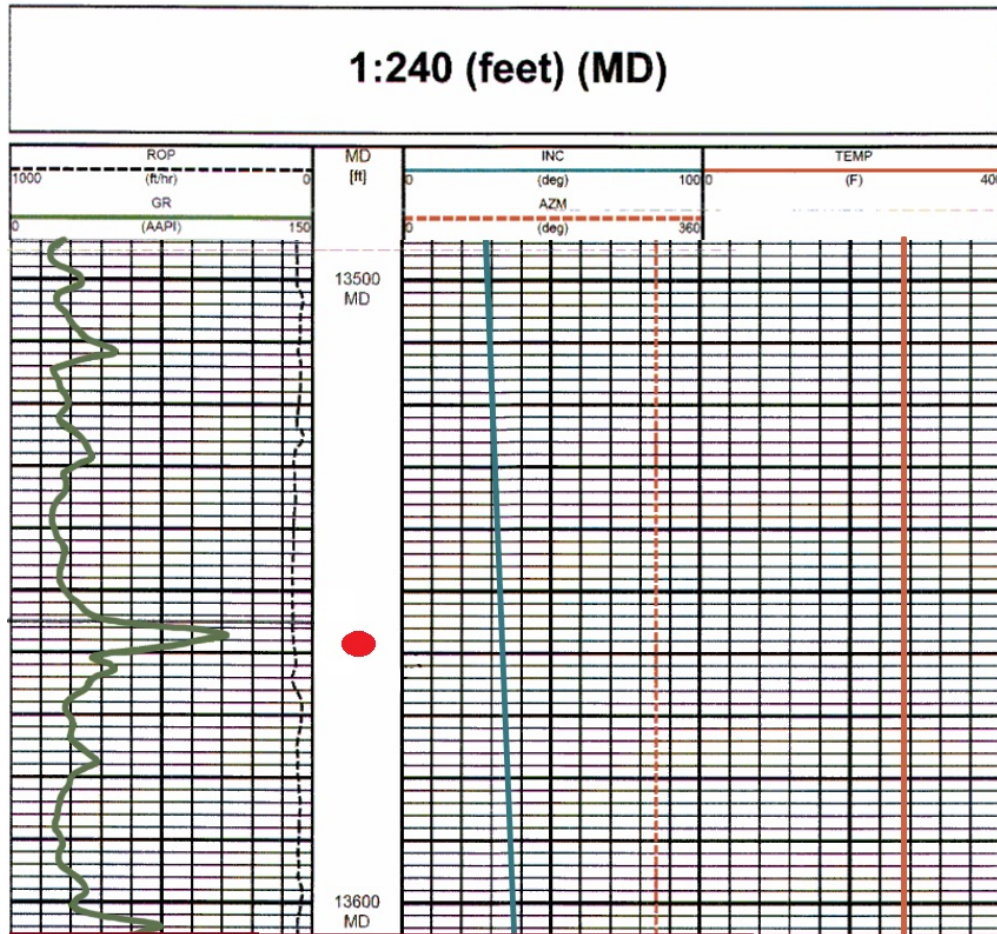
Figure 3.2: Well log for the Eagle Ford Formation of the reservoir sample. The red dot is indicating the sampling area (depth 4130 m MD) showing a raised Gamma Ray values (GR, green line). The red line shows the reservoir temperature in °F, which is 132°C.

3.4 AFM PF-QNM

3.4.1 Preparation

The sample preparation for AFM PF-QNM is rather extensive as the surface need to be extremely smooth with average roughness values of 100 nm (Kumar et al., 2012). The sample is cut into an approximate size of 7 x 7 x 3 mm (l x w x h) and attached to a small metal disc. Then, the sample is polished stepwise from 300 to 3000 grid. It follows broad beam argon ion milling of spots in the size of 1 mm^2.

3.4.2   Principle of AFM PF-QNM

PeakForce Quantitative Nanomechanical Mapping in atomic dorce Microscopy mode allows the acquisition of Young's modulus, deformation, adhesion force, dissipation, peak force error and surface height in real-time. This information is obtained through force-distance curves. At every measuring spot, the tip approaches the sample. When tip and sample get in contact a force is applied causing deformation of the sample (Figure 3.3). When the maximum peak force is reached, the tip is retracted from the sample. During the retraction, the tip interact with the sample causing the adhesion force. The energy dissipation is derived from the integral value between approach and retraction. The DMT modulus, which can be set equal to the Young's modulus in this study, is derived from the slope of the retraction curve.
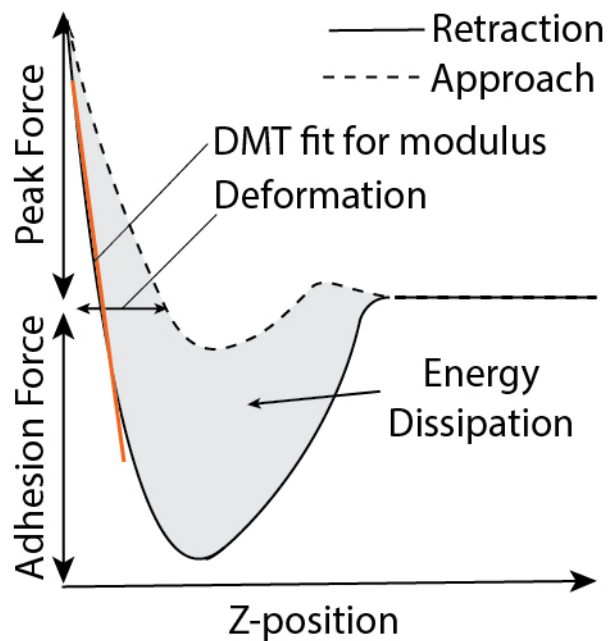
Figure 3.3: Load Displacement Curve indicating the approach (dashed line) and the retraction (solid line). The orange line shows the DMT fit for the calculation of the modulus.

3.4.3   Device and Steps

The sample preparation is followed by the PF-QNM Mapping. A detailed workflow can be seen in figure 3.4. After the laser alignment follows the calibration of sapphire.
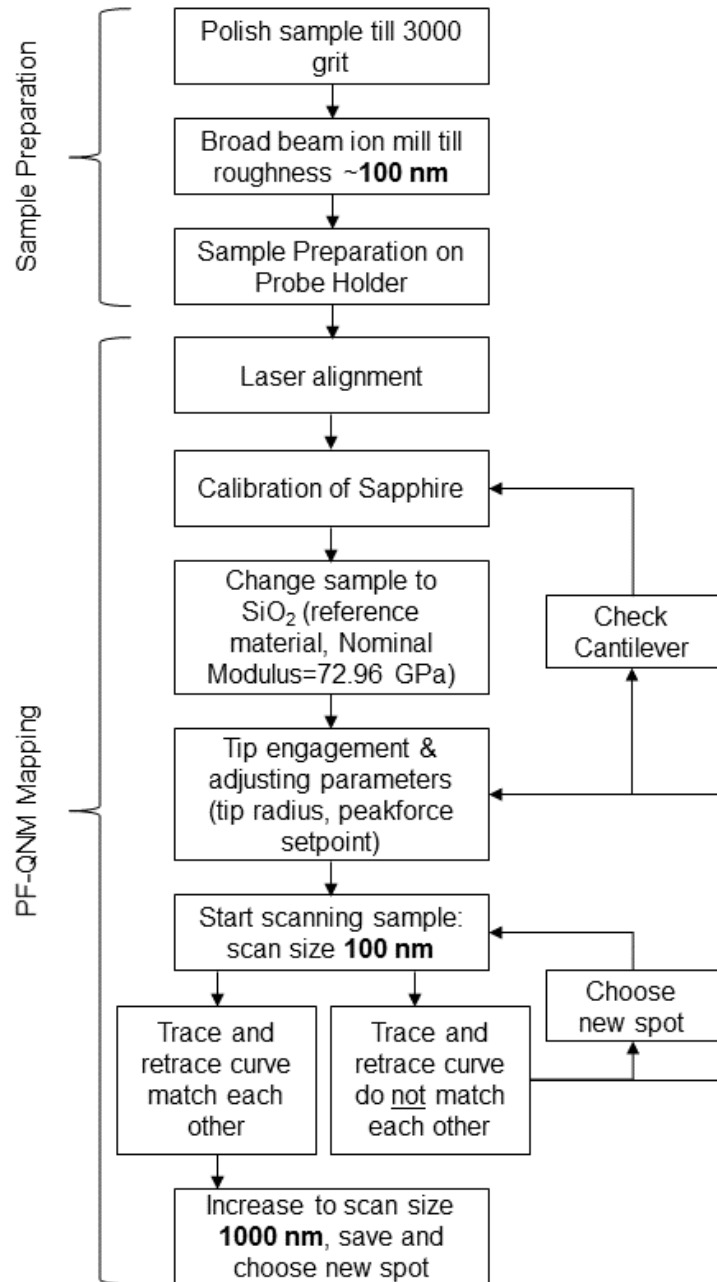
Figure 3.4: Flow chart of AFM PF-QNM mapping showing the sample preparation and the PF-QNM mapping steps.

In order to calibrate the device, the expected modulus range is required. Materials with a modulus of up to 100 GPa can be detected (Li et al., 2018). The results from XRD-Testing reveals the dominant minerals, which can be compared with table 2.1 for the single components and table 2.2 for the results of previous studies on the EF formation. The results from previous studies indicated

that a modulus range of 10 GPa <E <100 GPa is most suitable (Wilkinson et al., 2015; Eliyahu et al., 2015; Li et al., 2018). A diamond tip DNISP with a spring constant of 229 N/m is used to cover the modulus range.

The calibration follows a relative method of sapphire, which requires a standard sample of known Young's modulus. The tip radius that corresponds to a certain depth of deformation is measured. This way an "effective" tip end radius can be estimated. The measured modulus is corrected on a reference sample to avoid errors by considering the effective tip-surface area of contact. Calibration parameters that need to be determined are the deflection sensitivity, the spring constant and the tip radius. First, the deflection sensitivity is calibrated. The reference sample is loaded and the PeakForce setpoint is adjusted to keep the deformation between 5 and 10 nm. This allows for the estimation of the spring constant. The tip radius is adjusted, so that the measured modulus is close to the expected modulus. The average deformation is recorded before the sample is switched to the reference sample which is silicon dioxide with a nominal modulus of 72.96 GPa. The tip engagement is tested and the parameters such as tip radius and PeakForce setpoint are adjusted. The Poisson's ratio is set to a constant value of 0.3 and later adjusted.

The scanning starts with a small scan size of 100 nm before it is increased. If trace and retrace curve match each other, the scan size is increased to 1000 nm and saved as a result. If not, a new spot that shows less topographic features is chosen. If trace and retrace curve still do not match each other, the calibration parameters need adjustment and the cantilever should be tested.

The measurements were executed under ambient conditions with a standard cantilever holder for operation in air. A photograph for the device from the Institute of Bioengineering Research (IBER) from the University of Kansas can be seen in figure 3.5. The device is based on the control of the cantilever deflection. A feedback-loop imposes a setpoint to the maximum value of the deflection. The maximum force that is applied on the sample is therefore called peak force. The cantilever
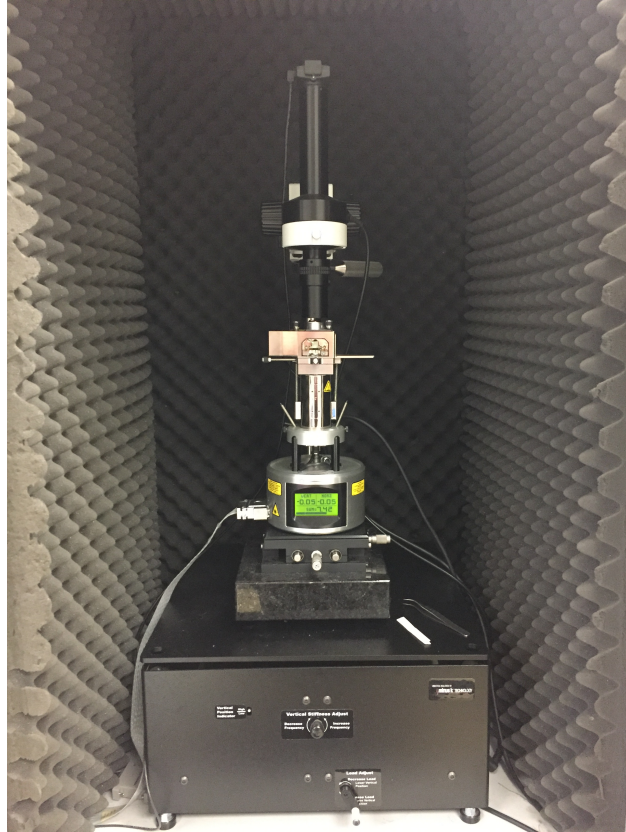
Figure 3.5: Photograph of the AFM at the Institute of Bioengineering Research (IBER) from the University of Kansas.

oscillates in Z-direction at 2 kHz imposed by a piezoelectric scanner. This scanner controls X,Y and Z displacements (Figure 3.6).

The force-distance curves and their analysis are acquired in real time (2000 per second) allowing for the simultaneous mapping of mechanical properties. The results show that the mapping has the same nano-metric lateral resolution as the topographic image.

3.4.4   Theory

The derivation of Young's modulus from AFM PF-QNM is derived from Hertz elastic model for spherical contact between the surface and the tip for homogeneous isotropic materials (Hertz, 1881). Therefore, the tip end radius is assumed to be a sphere, which is approaching the surface.
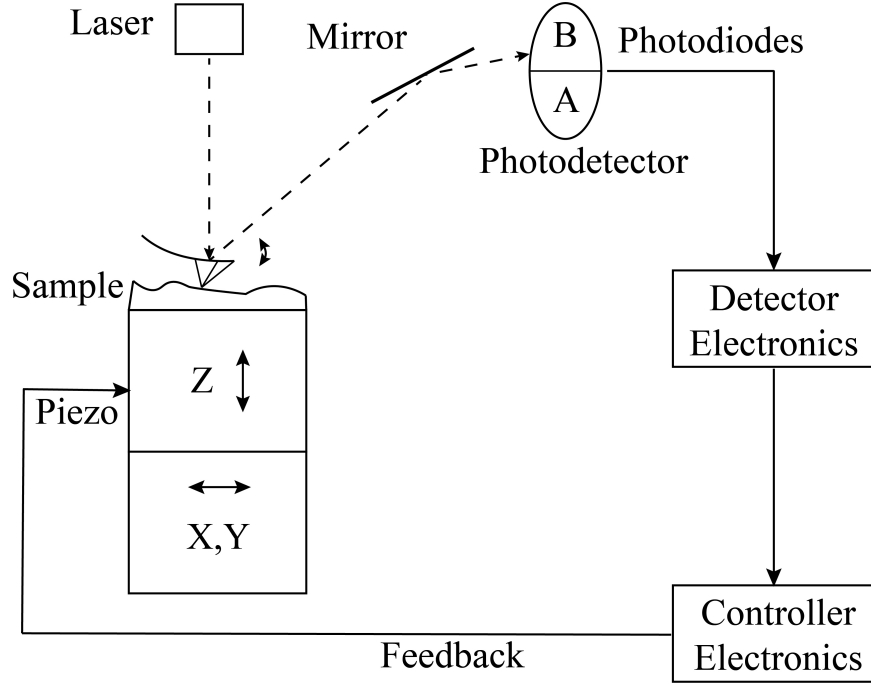
Figure 3.6: Schematics of the AFM PF-QNM testing device at the Institute of Bioengineering Research from the University of Kansas.

Following conclusion can be made from Hertz (1881):

$$F = \frac{4}{3} \frac{E}{1-v^2} \sqrt{R(\delta)^3} \qquad (3.1)$$

whereas F is the applied force, E is the Young's modulus, v is the Poisson's ratio, R is the tip end radius and δ is the deformation of the sample. It was found that the adhesion force between the tip and the probe has a significant impact on the result as molecular binding forces determine the properties of solids (Israelachvili, 2011). The Derjaguin-Muller-Toporov model (DMT) which takes the adhesion force in account was further developed (Derjaguin et al., 1975):

$$F_{tip} - F_{adh} = \frac{4}{3} E^* \times \sqrt{R(\delta)^3} \qquad (3.2)$$

22

where F_{tip} is the force applied on the tip and F_{adh} is the adhesion force. E^* represents the reduced modulus (DMT modulus). It is derived from the following correlation:

$$E^* = \frac{1}{\frac{1-v_s^2}{E_s} + \frac{1-v_{tip}^2}{E_{tip}}} \tag{3.3}$$

whereas v_s^2 and v_{tip}^2 are the Poisson's ratio of the sample and of the tip, respectively. E_s and E_{tip} are the Young's modulus of the sample and the tip, respectively. The diamond tip used for the application on carbonate-rich rocks has a Poisson's ratio of 0.07 and Young's modulus of 1141 GPa (Kumar et al., 2012). Based on the extremely low number of Poisson's ratio and the extremely high number of Young's modulus, it can be assumed that the term $(1 - v_{tip}^2)/E_{tip}$ equals to zero (Bruker-Corporation, 2011). This assumption leads to the following correlation:

$$F_{tip} - F_{adh} = \frac{4}{3}\frac{E}{1 - v^2} \times \sqrt{R(\delta)^3} \tag{3.4}$$

Here E and v represent the properties of the tested material.

3.4.5 Comparison AFM PF-QNM and Nanoindentation

Nanoindentation measures the geomechanical properties such as Young's modulus and hardness on a nano-scale. It can be performed on samples that are as small as drill-cuttings (Shukla et al., 2013; Bennett et al., 2015; Cała et al., 2017; Zhang et al., 2018). This technique measures discrete points on sample (Trtik et al., 2012). Several studies on shales (Liu, 2015; Gupta et al., 2018; Liu et al., 2018) and on limestone (Mighani et al., 2015) have been already performed. It is a measure of the resistance of a material to withstand applied compressive forces (Shukla et al., 2013). For every indentation, the reduced modulus E_r is determined from the slope of the unloading part of the load-displacement curve. It can be calculated using the following equation (Liu et al., 2018):

$$E_r = \frac{1}{2}\frac{\sqrt{\pi}}{\sqrt{A}}\frac{dP}{dh} \tag{3.5}$$

where A is the contact area and dP/dh (S) is measured from the the unloading slope. The Young's modulus is derived in the second step using the following equation (Bennett et al., 2015):

$$\frac{1}{E_r} = \frac{1 - v^2}{E} + \frac{1 - v_i^2}{E_i}$$

(3.6)

where v_i and E_i are the elastic Poisson's ratio and indentation modulus of the indenter.

A comparison between the principle of nanoindentation and the principle of AFM PF-QNM is shown in figure 3.7. The indentation depth of nanoindenters is up to 100 nm with a radius of impression at the surface of 13 μm (Shukla et al., 2013). Therefore, the deformation at each spot is permanent. The preparation of the sample is similar to the preparation for AFM PF-QNM. The sample is polished and ion milled until the average surface roughness is $\pm$ 10 μm (Shukla et al., 2013).

3.4.6 Surface Roughness

The surface roughness can be statistically evaluated (Zhao et al., 2019; Li et al., 2020). The evaluation ensures that the sample roughness is in the optimal range for AFM PF-QNM testing, as this technique requires a smooth surface.

The mean surface roughness R_a is calculated using the following equation:

$$R_a = \frac{1}{N_x N_y} \sum_{i=1}^{N_x} \sum_{j=1}^{N_y} |r(i,j)|$$

(3.7)

where N_x and N_y are the number of scanning points (here: 256 x 256 matrix), $r(i,j)$ is the height of the surface on the (i,j) measuring point. Another parameter to evaluate the surface roughness is the mean square roughness R_q, which is indicating the degree of change the standard deviation.
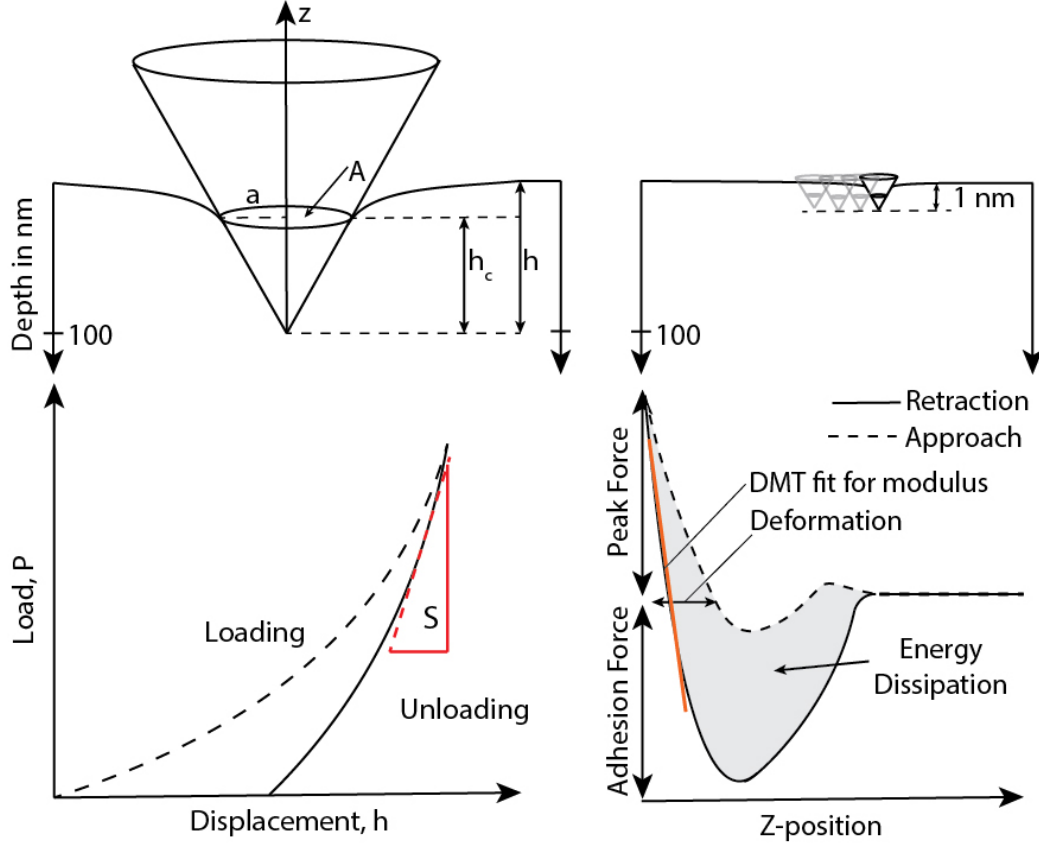
Figure 3.7: Schematic of the comparison between nanoindentation (left) and AFM PF-QNM (right). The upper part of the figure shows the comparison of the indentation depth. The indentation depth of nanoindentation is up to 100 nm, where a is the radius of contact, h is the displacement and h_c is the contact displacement. The indentation depth for AFM PF-QNM is 100 times smaller showing 1 nm depth. The modulus for nanoindentation is determined from the unloading slope of the load-displacement curve.

It can be calculated as follows:

$$R_q = \sqrt{\frac{1}{N_x N_y} \sum_{i=1}^{N_x} \sum_{j=1}^{N_y} r(i,j)^2} \tag{3.8}$$

The skewness R_{sk} shows the symmetry of the height distribution. It is normally distributed if the value equals to zero. For negative values, the distribution is biased to the left side and for positive values to the right side. It is calculated as follows:

$$R_{sk} = \frac{1}{N_x N_y} \sum_{i=1}^{N_x} \sum_{j=1}^{N_y} r(i,j)^3 \tag{3.9}$$

Another parameter is the kurtosis R_{ku}. It is a shape parameter for the uniformity, whereas a value equals to zero indicated normal distribution. For negative values, the waveform is flat and for positive values peaked. It can be calculated using the following correlation:

$$R_{ku} = \frac{1}{N_x N_y} \sum_{i=1}^{N_x} \sum_{j=1}^{N_y} r(i,j)^4 \qquad (3.10)$$

The surface roughness can be further evaluated calculating the maximum profile peak height R_p, which shows the highest peak of the surface:

$$R_p = \frac{1}{N_x N_y} \sum_{i=1}^{N_x} \sum_{j=1}^{N_y} \mid max \times r(i,j) \mid \qquad (3.11)$$

The opposite is the minimum profile valley depth R_v, which shows the lowest valley of the surface:

$$R_v = \frac{1}{N_x N_y} \sum_{i=1}^{N_x} \sum_{j=1}^{N_y} \mid min \times r(i,j) \mid \qquad (3.12)$$

The overall maximum height R_t of the profile can be derived from the absolute values between the lowest and the highest peak:

$$R_t = R_p + R_v \qquad (3.13)$$

Artifacts can be engendered by a rough surface, as the information derived from the tip-sample is strongly affected by the topography. When evaluating the surface roughness, it is also important to consider the area of contact between the surface of the tip end and the sample. A raster of 256 x 256 indentations in the size of 1 μm x 1 μm has been conducted at each spot. Thus, the spots have 3.91 nm distance to each other with an average deformation of 1.9 nm. The area of contact needs to be considered in relation to the distance between the single indentations. The area of contact radius can be evaluated using the following equation (Huang and Misra, 2012):

$$\delta_n = \frac{a^2}{R} \qquad (3.14)$$

26

where a is the contact surface radius and R is the radius of the tip end. The radius of contact is approximately 3.6 nm. Oversampling takes place, which, however, is negligible due to an elastic deformation of carbonate-rich rock.

3.4.7 Below Surface Area Influence

The results of the measurement are affected by anisotropy, especially hydraulic fractures and their propagation. The orientation of clay minerals will strongly affect the results. The measured value will be determined by the mineralogy, organic matter, texture and pore space. Therefore, what lies directly below the tested surface area will influence the result, even though the indentation depth is only 1 nm. According to Lambe and Whitman (1969), Boussinesq established a model for linear-elastic materials where Hook's law is valid. Figure 3.8 shows the stress in a semi-infinite solid. The stress is caused by surface pressure which is leading to a superposition of pressure in the area below the surface. The influenced area below the surface can be twice the area of contact in depth (Lambe and Whitman, 1969).
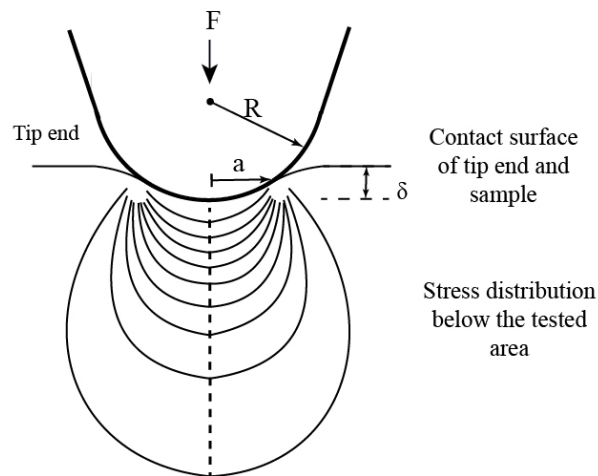

Figure 3.8: The applied force F is leading to a stress distribution in the subsurface. The contact surface of the tip end and sample shows the contact surface radius a, the radius of the tip end R and the deformation δ.

Underlying minerals, organic matter, texture and pore space will influence the tested material on

the surface (Figure 3.9). The largest influence will be caused by pore space and organic matter. The absence of a material or a material with a very low strength will lead to a higher deformation on the surface. A stiff mineral such as quartz will lead to a smaller deformation on the surface. Dickinson et al. (2020) found that pressure and temperature will have an impact on the adhesion force as the interaction between oil and mineral phases increases the adhesion force when the temperature is increased. The adhesion force decreases with increasing pressure (Dickinson et al., 2020). The influence of the adhesion force and the grain-to-grain interactions are important to consider for the evaluation of AFM PF-QNM measurements.
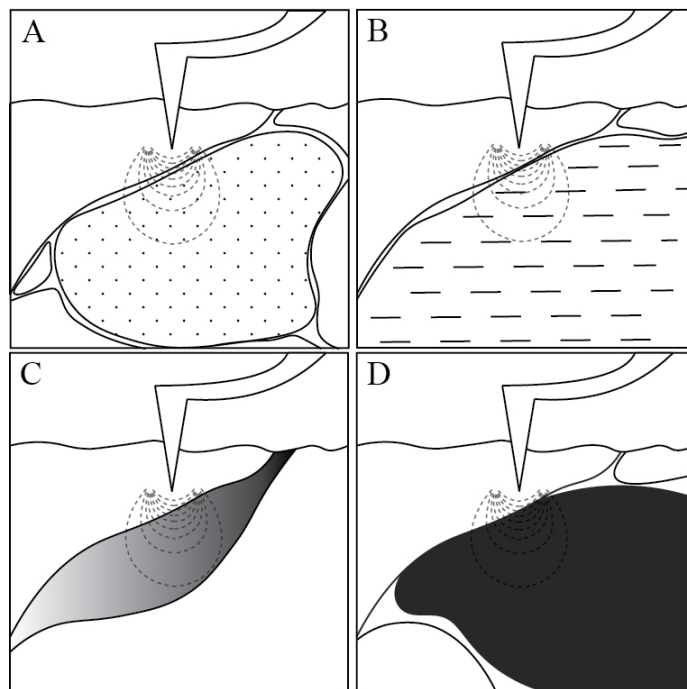
Figure 3.9: Influence of the area below the surface showing different possibilities where a quartz grain (A), a clay mineral (B), pore space (C) or organic matter (D) is below the tested material.

3.4.8 Iterative Model and Boundary Conditions

One of the main disadvantages of AFM PF-QNM is that it does not calculate the Poisson's ratio. For the testing the Poisson's ratio is set to a value of 0.3 (Li et al., 2018). However, the Poisson's ratio changes with the material properties and depends on the Young's modulus. An iterative model that solves for Poisson's ratio in dependency of Young's modulus has been developed. To develop

this model, equation 3.4 has been solved for the Young's modulus and implemented in the novel model:

$$E = (F_{tip} - F_{adh})\frac{3}{4}(1 - v^2)\frac{1}{\sqrt{R(\delta)^3}} \tag{3.15}$$

The equation is the initial expression (Figure 3.10). The range for Poisson's ratio is set to values between 0.1 and 0.4 based on the expected material properties and reported values from the literature (Gercek, 2007).
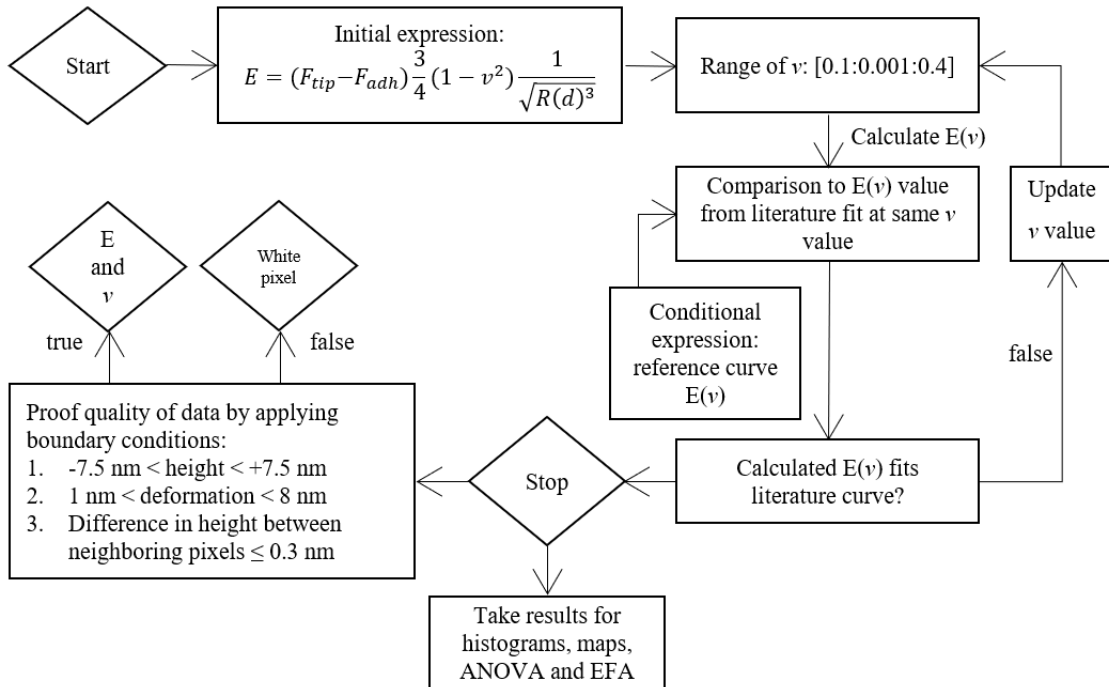
Figure 3.10: Work flow to develop the iterative model.

A specific correlation between the static Young's modulus and the Poisson's ratio for the EF formation is required. Values for the correlation were derived from triaxial tests in the literature (Enriquez-Tenorio et al., 2019; Jansen, 2014). The measured Young's modulus derived from true triaxial testing of this study is part of the correlation. A best fit quadratic correlation has been used. The reference curve represents the conditional expression. If E(v) fits the literature curve, the iteration stops. Otherwise the Poisson's ratio value is updated. The results are taken for the histograms, maps, ANOVA and EFA and represent the results for the AFM PF-QNM testing.

Boundary conditions are applied to proof the quality of the data. The height was set between -7.5 nm and +7.5 nm to exclude extreme troughs and peaks. Studies reported that data which show more than 10 nm difference in height, were filtered out (Wilkinson et al., 2015). However, as the Young's modulus does not follow the height with a difference in height of 15 nm, the boundary condition has been adjusted. The deformation for this material is expected to be between 1 nm and 8 nm, whereas 1 nm would indicate a stiff material such as quartz and 8 nm a ductile material such as organic matter. Previous studies on organic material filtered out data that were not in the range of 3.23 nm and 8.05 nm (Li et al., 2018). In this study all components of the rock were tested, which leads to smaller deformations and an adjustment of the boundary condition. The ensure that two neighboring pixel do not deviate too much, the boundary condition from previous studies for the difference in height between neighboring pixel smaller of equal to 0.3 nm, has been applied (Wilkinson et al., 2015). If one or more boundary conditions are not fulfilled, the Young's modulus shows as a white pixel in maps and the result is excluded. The boundary condition that the Young's modulus lies between 0 GPa and 100 GPa has not been applied (Eliyahu et al., 2015). The Young's modulus of calcite and quartz are expected to be lower than 100 GPa (Simmons and Wang, 1971). However, Pyrite that was found in the optical microscopy analysis yields to extremely high values of Young's modulus of 250 GPa to 310 GPa (Simmons and Wang, 1971).

Especially for changes in morphology that are too high, which occurs on the edges of grains, the Young's modulus follows the height and the uncertainty is increased. The diamond DNISP-HS tip leads to uncertainties of 15% for the range of 10 GPa to 70 GPa on shale samples based on previous studies (Eliyahu et al., 2015). For Young's modulus values of less than 10 GPa, the uncertainty is approximately ± 2 GPa (Eliyahu et al., 2015).

3.5 Statistical Methods

3.5.1 Analysis of Variance

Analysis of Variance (ANOVA) is a statistical method that tests the difference between group means and determines whether group means are equal or not. Thus, it tests the null hypothesis that samples are drawn from a population that has the same mean. It is tested against the alternative hypothesis stating that the population means are not the same. For very low p-values, the null hypothesis is rejected. ANOVA is applied to predict if the 15 measured spots are drawn from the same population. This would indicate that the same components have been tested or if the composition changes, indicating heterogeneity. It tests the difference between groups in order to explain the total sum of squares (SST). This can be explained by the variation of group means (SSR) from the overall mean and the variation in each group (SST) from the group mean:

$$\underbrace{\sum_{ij}(y_{ij}-\bar{y}_{..})^2}_{SST} = \underbrace{\sum_j n_j(\bar{y}_{.j}-\bar{y}_{..})^2}_{SSR} + \underbrace{\sum_{ij}(y_{ij}-\bar{y}_{.j})^2}_{SSE} \qquad (3.16)$$

where y is the variation and n_j is the sample size for the jth group. The variation between the groups in relation to the variation within a group is compared to determine, whether the means are derived from the same population, indicating that the same material has been tested. The variation between the groups in relation to the variation within a group would show high values, if for example only the same quartz grain has been tested.

3.5.2 Exploratory Factor Analysis

Exploratory factor analysis is applied to simplify the complex model comprising 15 spots with 256 x 256 measurements, respectively. It is a multivariate statistical tool that is commonly used in social sciences. However, it has also broad applications in petroleum engineering (Andrade et al., 1997; Jain et al., 2013). The measurements are the results for Young's modulus at each tested

spot. It is used to determine the number of underlying factors, which cause compositional changes (Maskey et al., 2018). The variance of each indicator is derived from the covariance matrix, which is the input of the analysis. The variance is divided into two parts, the common variance and the unique variance. The common variance is the variance accounted for by the factor and estimated on the basis of the variance shared with other indicators. The unique variance is a combination of the reliable variance specific to the indicator, which would be for example a systematic influence on only one indicator and the random error variance, which measures the error or the unreliability in the indicator (Brown, 2015).

Overall, the multivariate statistical tool reduces the large data set to a smaller set of factors. It determines if unmeasured factors could be determined from the variance/covariance matrices. This represents the variance of the data set by factors. The following calculations have been used to perform the EFA (Kim et al., 2017):

$$X = L \times F + R \tag{3.17}$$

$$
\begin{pmatrix} x_1 \\ x_2 \\ ... \\ x_p \end{pmatrix} =
\begin{pmatrix} l_{1,1} & l_{1,2} & \cdots & l_{1,m} \\ l_{2,1} & l_{2,2} & \cdots & l_{2,m} \\ \vdots & \vdots & \ddots & \vdots \\ l_{p,1} & l_{p,2} & \cdots & l_{p,m} \end{pmatrix} \times
\begin{pmatrix} f_1 \\ f_2 \\ ... \\ f_m \end{pmatrix} +
\begin{pmatrix} r_1 \\ r_2 \\ ... \\ r_m \end{pmatrix} \tag{3.18}
$$

where X indicated the measured data with p variables, L represent the factor loadings, F are the common factors for m numbers of factors and R indicates the residual errors. The model is valid if $m \leq p$ (Kim et al., 2017). Equation 3.17 is solved for L, the factor loadings. Assumptions about common factor terms and the independence of error lead to the determination of eigenvalues $(\lambda_1, \lambda_2, ..., \lambda_p)$ and the corresponding eigenvectors $(e_1, e_1, ..., e_p)$ determined from the covariance matrix (Kim et al., 2017). The number of common factors, which represent the complex model, are determined from the scree plot. It is a plot of eigenvalues in descending order versus the number

of components (Fabrigar and Wegener, 2012). The variance of X is determined from the following correlation (Kim et al., 2017):

$$Var(x_i) = l_{i1}^2 Var(f_1) + l_{i2}^2 Var(f_2) + ... + l_{im}^2 Var(f_m) + Var(r_i) \qquad (3.19)$$

$$Var(x_i) = \underbrace{l_{i1}^2 + l_{i2}^2 + ... + l_{im}^2}_{communality} + \underbrace{\psi_i}_{specific\,variance} \qquad (3.20)$$

where the *communality* represents within each measured variable how well the common factors explain the total variance and the *specific variance* indicated parts that are not explained by F (Kim et al., 2017).

3.6 True Triaxial Testing

3.6.1 Preparation

Triaxial testing has many refinements, whereas true triaxial testing is one of it. The setup requires a 4 cm cubic specimen. The sample is cut in several steps in order to guarantee the preparation of the cube. This need careful implementation as the sample material is brittle. After the preparation all longitudinal sides are grounded to avoid breaking of the sensitive corners. The sample is completely covered with graphite spray to improve the contact between the sample and the anvils.

The loading can be applied hydrostatically or independent of three pairs of opposite faces to activate the principal stresses. The maximum principal stress σ_1 is the overburden stress, σ_2 is the intermediate principal stress and σ_3 is the minimum principal stress ($\sigma_3 < \sigma_2 < \sigma_3$). For this test the stress is applied hydrostatically, where $\sigma_3 = \sigma_2 = \sigma_3$.

3.6.2 Principle

The geomechanical properties are calculated from the seismic velocities that are measured and averaged over the entire length of the specimen. Ultrasonic pulse transmission technique is used for the propagation of elastic waves. The true triaxial testing apparatus measures the compressional wave (p-wave) and the shear wave (s-wave) velocities in a 3D stress space. The p-wave and two orthogonally polarized s-waves are measured in X-, Y- and Z-direction (Figure 3.11). The Z-direction is normal to the stratification, whereas X- and Y-direction are parallel to the stratification. For each loading increment, three p-waves and six s-waves are measured. The amplitude extraction of the shear wave splitting is crucial as is is a measurement of anisotropy (Motra and Wuttke, 2016; Riazi et al., 2017).
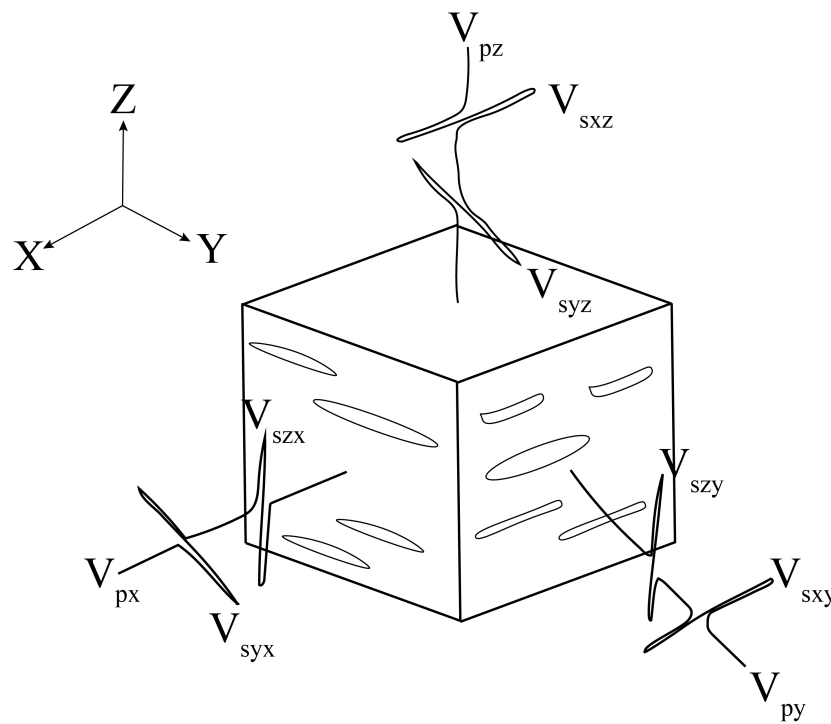

Figure 3.11: Schematic of p- and s-waves propagation the cubical sample for true triaxial testing.

3.6.3 Device and Steps

The true triaxial testing apparatus at Kiel University, Germany, works with six anvils affecting each side of the cubic sample (Figure 3.12). Attached to each anvil are two pins, which measure the change of each side of the sample during the test. Figure 3.13 shows photographs of the triaxial testing apparatus that has been used. The closeup view shows the sample covered with graphite spray attached to the anvils on three sides. The arrow on the sample marks the X-direction.
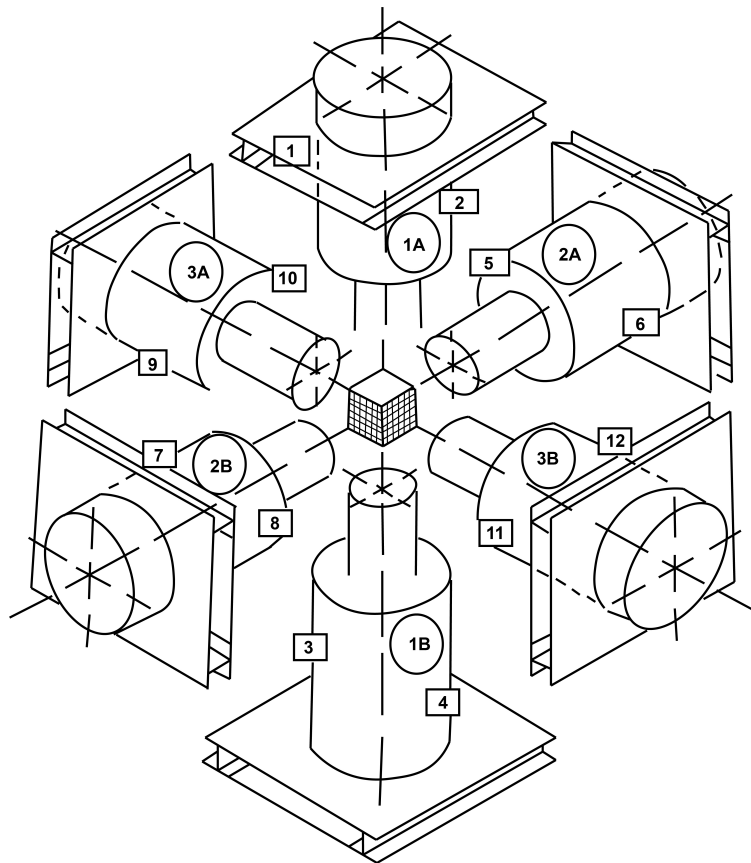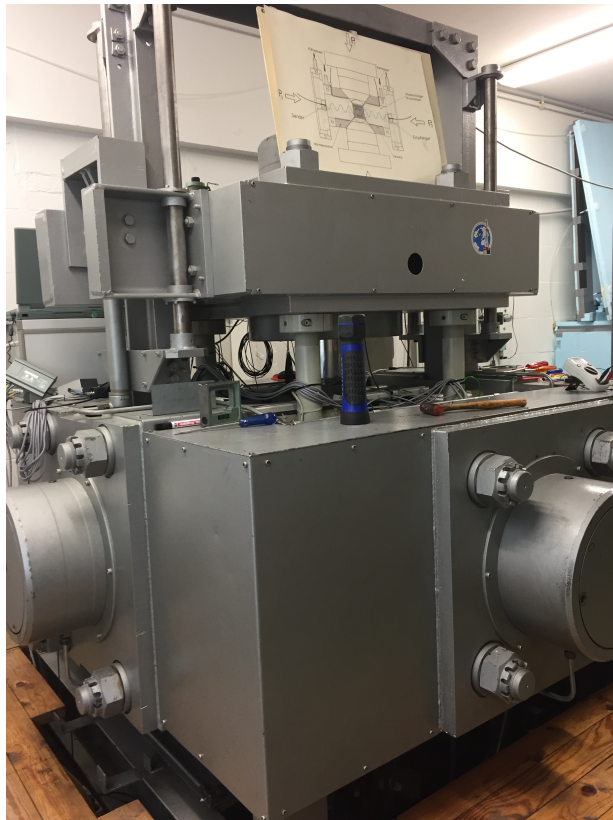

Figure 3.12: Schematic of the true triaxial testing apparatus showing the numbered anvils in circles and the numbered pins in squared. 1A and 1B indicate Z-direction, 2A and 2B show the Y-direction and 3A and 3B represent the X-direction. The pins measure the change of each side of the sample during the test. Pins 1 and 2 measure the change for anvil 1A, 3 and 4 for anvil 1B, 5 and 6 for anvil 2A, 7 and 8 for anvil 2B, 9 and 10 for anvil 3A and 11 and 12 for anvil 3B.

The pressure varies from 8 MPa to 50 MPa at a constant temperature of 41°C. The test was part of a series of tests that has been performed at lower temperatures than the actual reservoir temperature. The effect of the temperature on the mechanical behavior of the minerals will be minor. However,

the temperature could have an effect on the bitumen. The pressure range from 8 MPa to 50 MPa has been applied as the effect of pressure is insignificant for higher confining stresses. At low confinements micro-cracks are closed. These cracks are drilling induced and do not represent the properties of the tested material. Therefore, the Young's modulus from true triaxial testing at higher confining pressures needs to be compared to the results from AFM PF-QNM, as this device only considers a narrow region with a sampling size too narrow to capture the closure of micro-cracks.

(a) True triaxial testing apparatus

(b) True triaxial testing apparatus closeup view

Figure 3.13: Setup of the true triaxial testing apparatus at Kiel University, Germany.

3.6.4 Theory

The true triaxial testing apparatus measures one p-wave and two s-waves in X-,Y- and Z-direction, respectively. In order to calculate the mechanical properties, the bulk density ρ needs to be calculated using the following equation:

$$\rho = \frac{m_d}{V} \tag{3.21}$$

where m_d is the dry weight of the sample and V is the sample volume. The Poisson's ratio, dynamic Young's modulus E_{dyn} and dynamic bulk modulus K_{dyn} are calculated from Hook's law (Mavko et al., 2009; Blake and Faulkner, 2016):

$$v = \frac{1}{2}\left(\frac{V_p^2 - 2V_s^2}{V_p^2 - V_s^2}\right) \tag{3.22}$$

$$E_{dyn} = \rho \times V_s^2 \left(\frac{3V_p^2 - 4V_s^2}{V_p^2 - V_s^2}\right) \tag{3.23}$$

$$K_{dyn} = \rho \times (V_p^2 - \frac{4}{3}V_s^2) \tag{3.24}$$

where V_p and V_s are the p-wave velocities and the s-wave velocities, respectively.

In order to compare the static Young's moduli results from AFM PF-QNM with the results from true triaxial testing, the static mechanical properties are calculated from the volumetric strain and stress relationship for the static bulk modulus K_{stat}:

$$K_{stat} = \frac{\Delta\sigma}{\Delta\varepsilon_v} \tag{3.25}$$

where σ is the effective stress in MPa and ε_v is the volumetric strain in percentage. The static bulk modulus can be converted to the static Young's modulus E_{stat} using the following correlation:

$$E_{stat} = 3 \times K_{stat}(1 - 2v) \tag{3.26}$$

The anisotropy for the p-waves is calculated for every loading increment using the following correlation (Motra and Stutz, 2018):

$$A = \frac{V_{p,max} - V_{p,min}}{V_{p,mean}} \times 100\% \qquad (3.27)$$

where A is the anisotropy. $V_{p,max}$ is the maximum, $V_{p,min}$ the minimum and $V_{p,mean}$ the mean p-wave velocity.

Chapter 4

Results and Discussion

Abstract

This chapter examines the geomechanical properties on different scales. In order to characterize the tested material, XRD and microscopical analysis have been performed. XRD quantifies the crystalline components, whereas microscopy considers the non-crystalline components and the structure. The characterization of the EF formation samples are followed by the results from AFM PF-QNM testing. An iterative model that solves for Poisson's ratio in dependency of Young's modulus has been applied. The surface roughness has been evaluated to ensure the quality of the data. As the results from AFM PF-QNM testing encompasses a large data set of measurements, statistical methods have been implemented to explain the relationship between the measurements and to explain the large data set by a smaller set of factors. These results have been compared to the results from true triaxial testing. The anisotropic nature of the material has been studied. Eventually a connection between the results from geomechanical testing from AFM PF-QNM on a nano-scale and true triaxial testing on a macro-scale have been drawn. The different scales from static and dynamic geomechanical testing were considered and play a decisive role in the evaluation.

4.1   XRD Analysis

XRD analysis has been performed on both samples as the elastic properties strongly depend on the mineralogy. The XRD spectrograms for the outcrop sample (Figure 4.1) and the reservoir sample

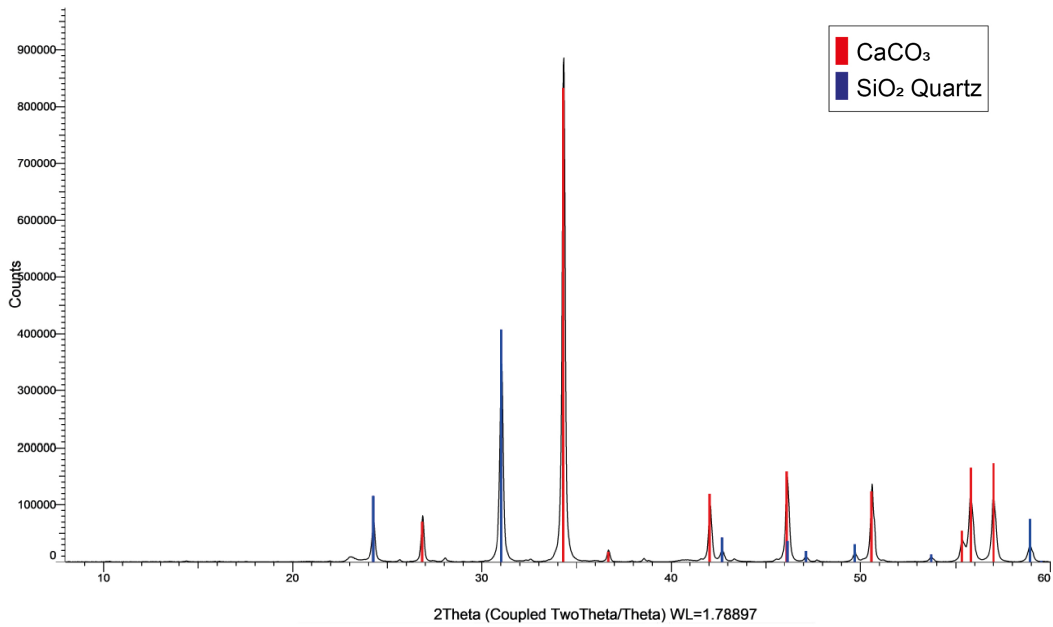(Figure 4.2) indicate that quartz and calcite are the main components.

Figure 4.1: XRD Analysis of the outcrop sample undergone AFM PF-QNM. Red peaks indicate the counts for calcite and blue peaks show the counts for quartz.
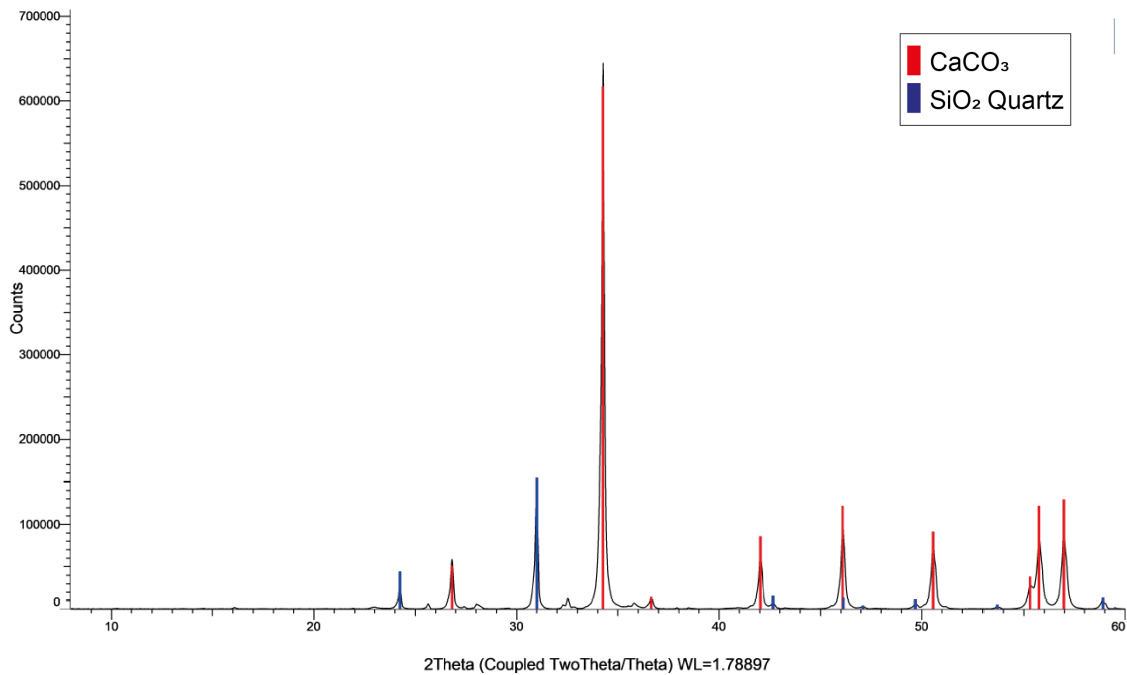

Figure 4.2: XRD Analysis of the reservoir sample undergone true triaxial testing. Red peaks indicate the counts for calcite and blue peaks show the counts for quartz.

The respective weight percentages are represented in table 4.1. The reservoir sample contains 36.1% quartz and 63.9% calcite. The outcrop sample contains approximately 10% more calcite with overall 26.6% quartz and 73.4% calcite.

Table 4.1: XRD analysis results for the reservoir and the outcrop sample

| Eagle Ford	Reservoir sample	Outcrop sample
Quartz (wt. %)	36.1	26.6
Calcite (wt. %)	63.9	73.4

4.2 Microscopical Analysis

The microscopical analysis shows the internal structure and characterizes non-crystalline material.

The sample for AFM PF-QNM shows two distinct intervals. One interval consists of thicker laminae of shaly organic-rich material. Within this structure kerogen particles, clay and isolated planktonic foraminifera were found. This interval is alternating with calcite-rich foraminifera layers. The matrix shows scattered pyrite along with calcite cement which consists of single crystals. Figure 4.3 shows four photomicrographs from this sample. Figure 4.3a shows the calcite-rich foraminifera layers in cross-polarized light and figure 4.3b in plane polarized light. The organic-rich material can be seen in figure 4.3c in plane polarized light. Figure 4.3d shows the entire chip on a larger scale. It clearly shows the layering of foraminifera alternating with shaly organic material. The orientation of the grains and the internal lamination are an indicator for anisotropy.

The sample for true triaxial testing shows a peloidal carbonate with few clays. It shows foraminifera-rich lamina along with scattered pyrite. The sample reveals bioturbations and little dolomite. The calcite cement of the matrix is polycrystalline. Figure 4.4 shows four photomicrographs from this sample. Figure 4.4a shows the foraminifera-rich lamina in cross-polarized light. The figures 4.4b and 4.4c show the foraminifera-rich lamina and clays in plane-polarized light with different scales. Figure 4.4d shows the foraminifera-rich lamina on a different spot in plane-polarized light.
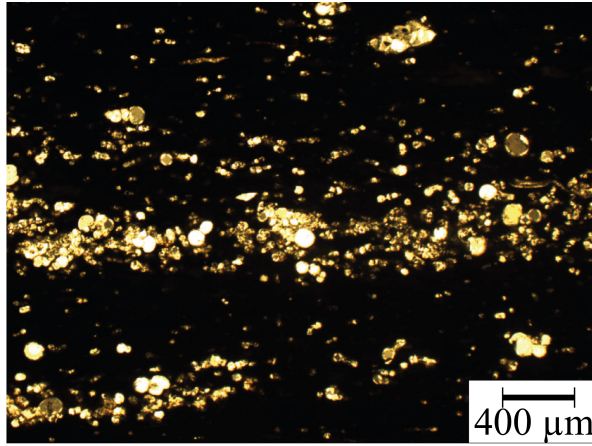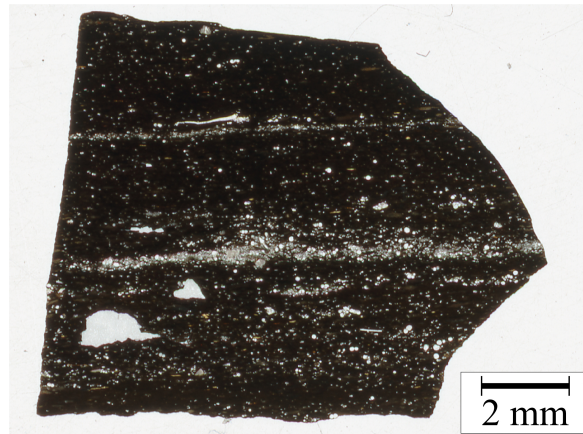
(a) Cross-polarized
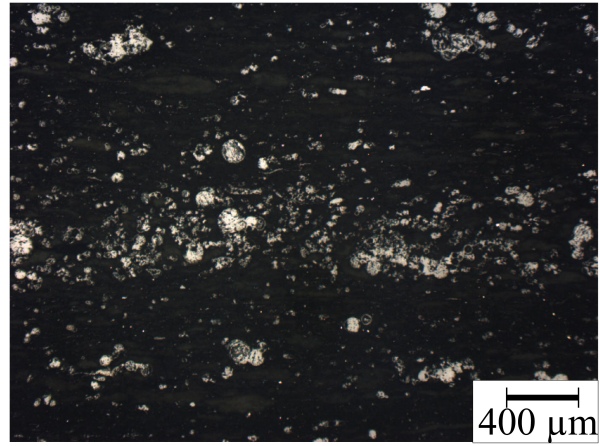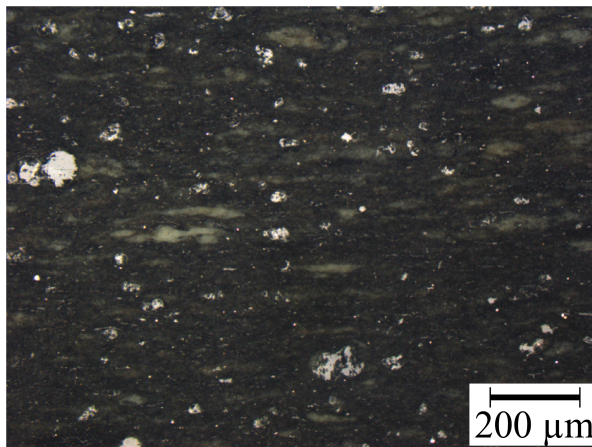
(b) Plane-polarized

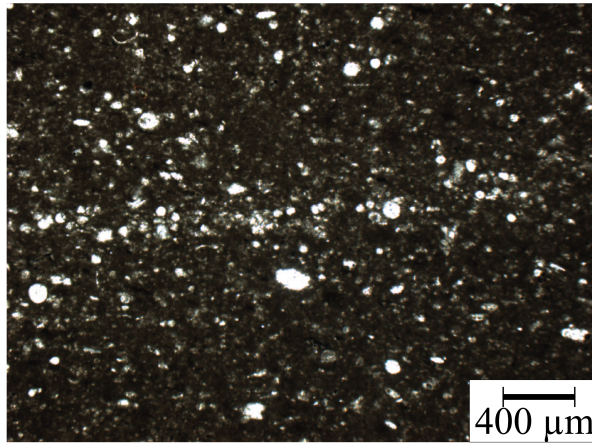(c) Plane-polarized

(d) Photo-micrograph

Figure 4.3: Transmitted light photomicrographs of polished thin sections for the sample from AFM PF-QNM.

4.3 AFM PF-QNM

4.3.1 Iterative Model

The iterative model (Figure 3.10) has been applied to determine the Poisson's ratio in dependency of the Young's modulus. Therefore, geomechanical reference data indicating Young's modulus and Poisson's ratio from the literature for the EF formation (Enriquez-Tenorio, 2016; Enriquez-Tenorio et al., 2016) in addition to the true triaxial testing result in this study have been taken as reference correlation between Young's modulus and Poisson's ratio.

(a) Cross-polarized
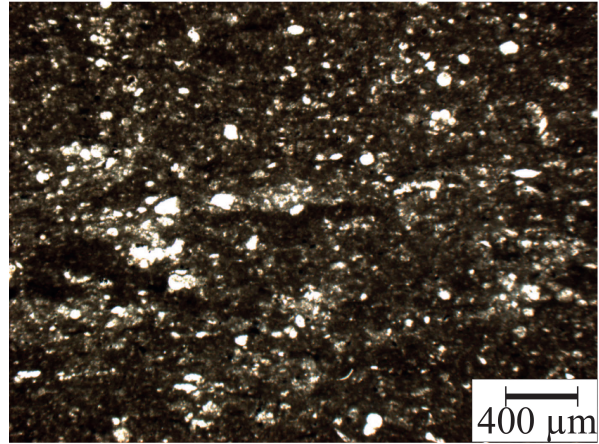
(b) Plane-polarized
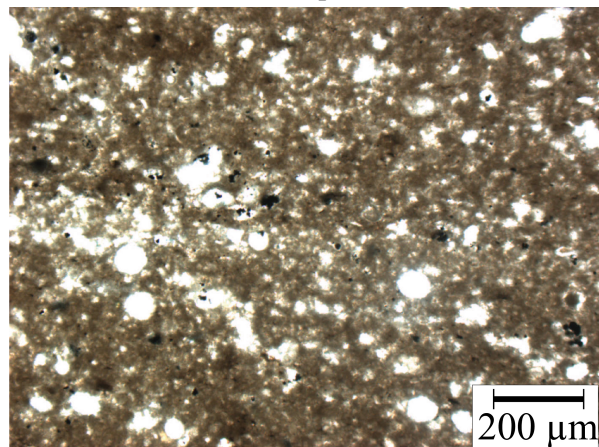
(c) Plane-polarized

(d) Plane-polarized

Figure 4.4: Transmitted light photomicrographs of polished thin sections for the sample from true triaxial testing.

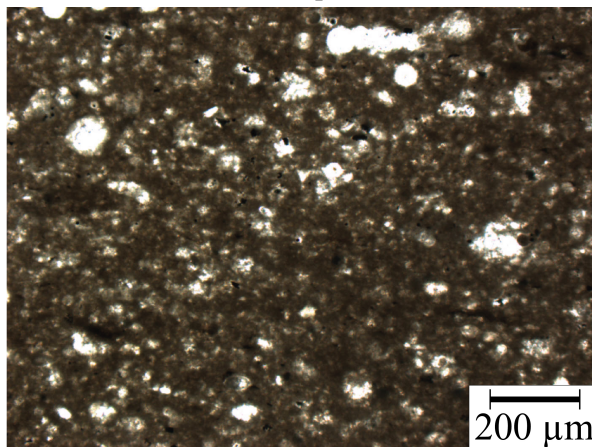Figure 4.5 shows the polynomial fit function for the reference data that were obtained from the literature. The accumulation of measured data at a Poisson's ratio of 0.12 can be explained by the minimum in quadratic fit, which has been chosen as best fit for the reference data. The fit is not forced to begin at zero leading to the accumulation of data points at a Poisson's ratio of 0.12 for data points that are roughly below 23 GPa.

The iterative model for one single data point is explained in figure 4.6. The blue line represents the quadratic fit through the reference data. The red crosses indicate the resulting value for Young's

Figure 4.5: Young's modulus versus Poisson's ratio: reference data for the iterative model indicated by black crosses. The red line i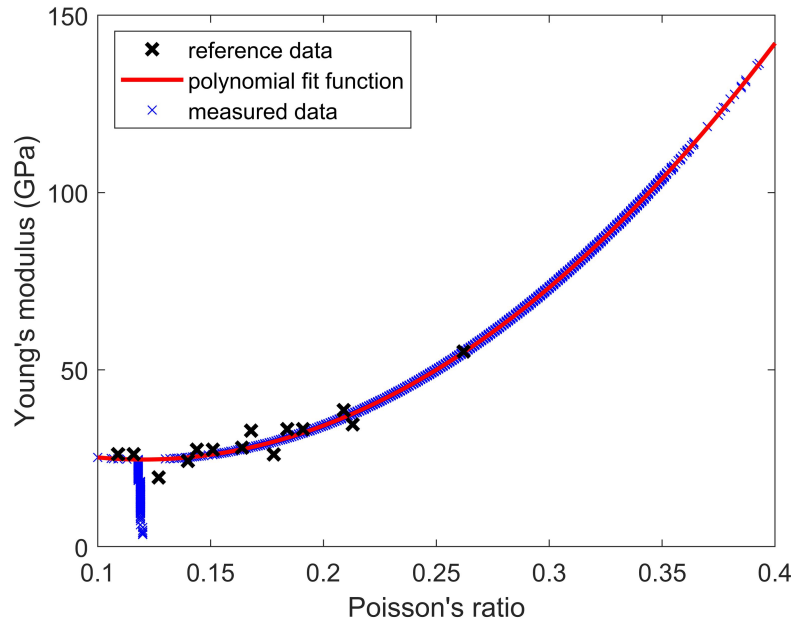ndicates the polynomial fit function and the blue crosses show the reevaluated algorithm from the measured data. The accumulation of measured data at a Poisson's ratio of 0.12 can be explained by the minimum in quadratic fit, which has been chosen as best fit for the reference data.

modulus for each Poisson's ratio from 0.1 to 0.4 with a step size of 0.001. The intersection of the measured data and the reference data (red crosses and blue line) represent the newly determined Poisson's ratio in dependency of Young's modulus. The new values reveal a Young's modulus of 47.27 GPa and and a Poisson's ratio of 0.24 for this exemplary measurement (instead of E=49.64 GPa and v=0.3). As the Poisson's ratio varies with Young's modulus, it also depends on the applied force on the tip, the adhesion force and the deformation.

Boundary conditions have been applied to ensure the quality of the data. Maps with applied boundary conditions can be seen exemplary for spot 5 in figure 4.7a for low values of Young's modulus and for spot 7 in figure 4.7b for high values of Young's modulus.
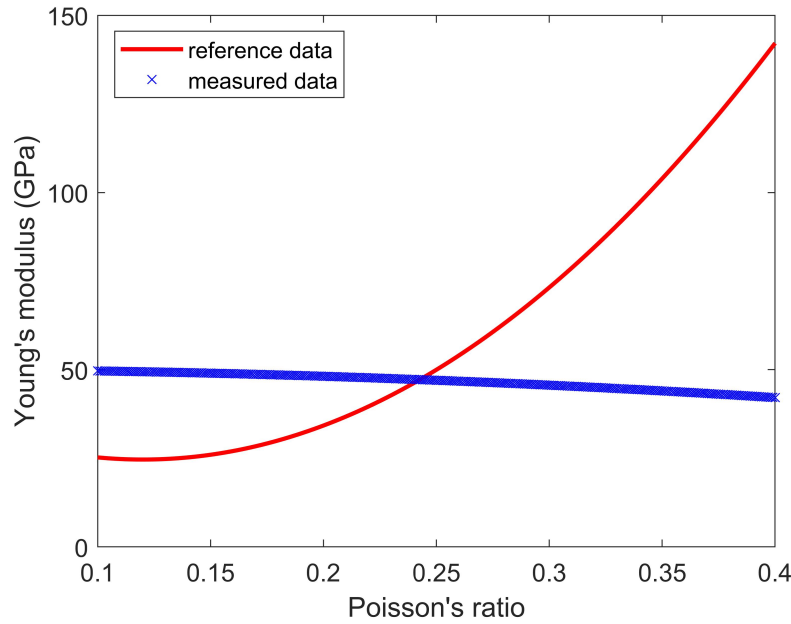
Figure 4.6: Young's modulus versus Poisson's ratio: fit for one data point from the model. The intersection between the reference curve (red line) and the measured data (blue line) represents the newly determined Young's modulus and Poisson's ratio. The old values were 49.64 GPa for Young's modulus and 0.3 for Poisson's ratio for one measurement. The iterative model determined a Young's modulus of 47.27 GPa and 0.24 for Poisson's ratio.

4.3.2 Surface Roughness

AFM PF-QNM is extremely sensitive to surface morphology variations. The required average surface roughness for AFM PF-QNM is 100 nm. In order to test the sample preparation prior to AFM PF-QNM testing, the sample was tested under the optical profilometer. Figure 4.8 shows an average surface roughness from optical profilometer measurements of 105.59 nm on the broad beam ion milled spot.

The surface roughness from AFM PF-QNM has been statistically evaluated using the equations 3.7 to 3.13. Table 4.2 shows the results for the 15 tested spots. The mean surface roughness R_a varies from 2.9 nm to 43.7 nm with an average of 9.4 nm. The standard deviation R_q varies from 3.8 to 62.5 nm. Liu et al. (2010) found that the standard deviation is more sensitive to surface roughness variations than the mean surface roughness, a trend that can be confirmed by this study. R_q shows higher values than R_a. The skewness R_{sk} varies from -1.7 to 1.6 with an average of 0.14, indicating
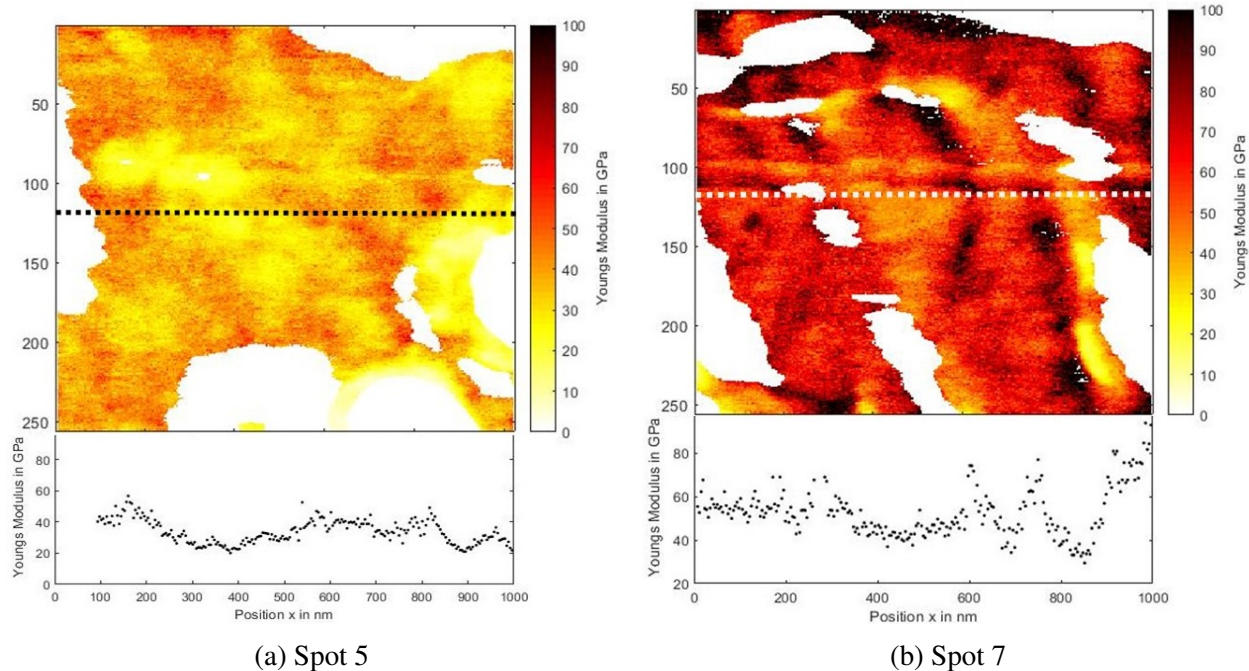
Figure 4.7: Distribution of Young's modulus for spot 5 (left) and for spot 7 (right) with applied boundary conditions showing the 256 x 256 raster of data points. White pixel indicate the absence of data where the boundary conditions have been applied.
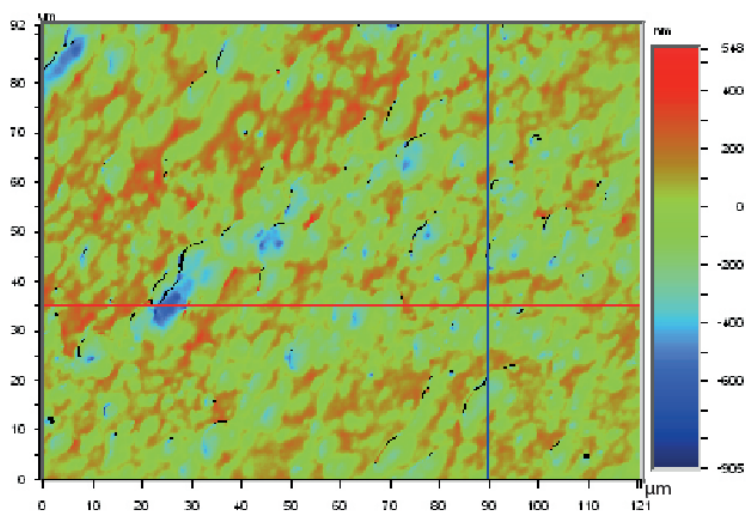
Figure 4.8: Optical profilometer showing a size of 92 x 121 μm^2 of the ion milled spot prior to AFM PF-QNM testing. The colorbar indicates the height in nm.

that the sample has slightly more peaks than troughs. The kurtosis R_{ku} shows values varying from 2.7 to 9.0 revealing a concentrated distribution. The maximum peak R_p shows a height of 120 nm for spot 2 and a maximum valley depth R_v of 280 nm for the same spot. This results in a maximum

Table 4.2: Evaluation of the surface roughness for 15 tested spots.

Spot	R_a	R_q	R_{sk}	R_{ku}	R_p	R_v	R_t
1	5.3	6.6	-0.4	3.2	19	27	46
2	43.7	62.5	-1.7	5.9	120	280	400
3	3.8	4.6	0.1	2.7	19	11	30
4	5.1	7.6	1.6	9.0	43	21	65
5	12.5	16.7	1.5	5.6	64	29	93
6	4.8	5.9	0.1	2.7	15	20	35
7	10.9	13.5	0.6	2.9	40	28	68
8	5.4	7.2	0.5	3.7	22	23	46
9	10.9	14.5	-0.6	4.1	34	56	90
10	15.9	20.0	-0.5	2.7	53	57	110
11	5.2	6.7	0.1	3.4	31	21	51
12	2.9	3.8	-0.2	3.2	12	12	24
13	4.5	5.8	-0.7	3.5	16	20	35
14	5.4	6.9	1.1	3.9	28	16	44
15	4.8	6.0	0.7	3.1	19	16	35

height R_t of 400 nm. The evaluation shows that spot 2 shows the strongest variation in height, which could result in errors during the measurement.

4.3.3   Geomechanical Maps

Overall, 15 spots have been tested for AFM PF-QNM. Each spot contains a matrix of 256 x 256 (=65,536) data points. The figures 4.9 to 4.16 show the distribution of Young's modulus as a map to reveal rock structures and as histogram.

Figure 4.9 shows the spots 1 and 2. Spot 1 shows few data points for the phase 0 to 25 GPa and intermediate data point for the phase from 50 to 100 GPa. The accumulation in data points is between 25 and 50 GPa. The histogram (Figure 4.9b) shows a bimodal distribution indicating a separation between the phase of smaller strength and higher strength. Spot 2 shows intermediate data points for the phases 0 to 25 GPa and 50 to 100 GPa. The accumulation is at values between 25 and 50 GPa. Spot 1 and spot 2 show the best fit for a gamma distribution as the results from both spots are shifted to the left indicating fewer high Young's modulus results.
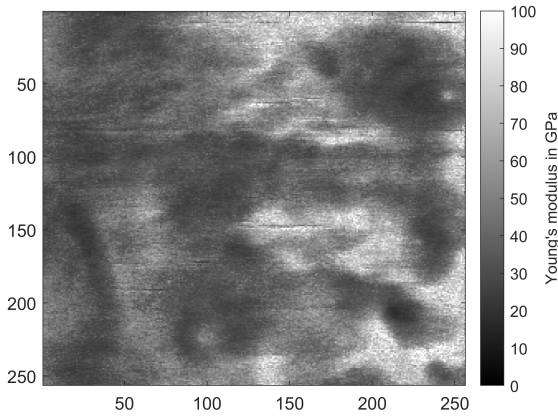
(a) Spot 1 map
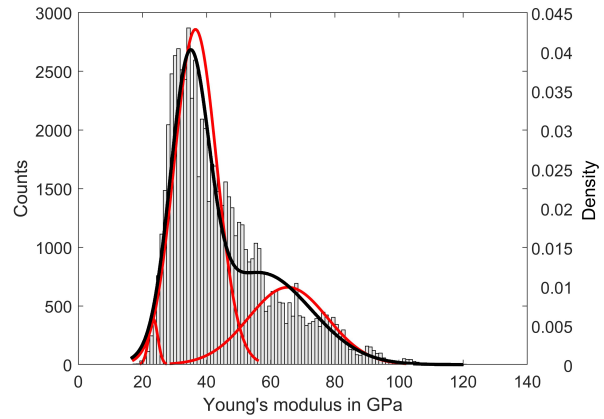
(b) Spot 1 histogram
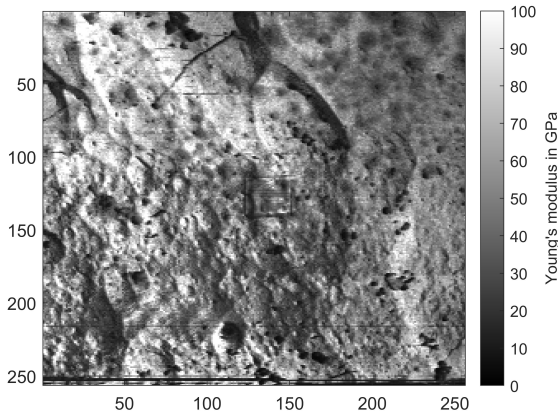
(c) Spot 2 map

(d) Spot 2 histogram

Figure 4.9: Distribution of Young's modulus on a map (left) and a histogram (right). The map on the left shows the 256 x 256 matrix, whereas dark colors indicate low values of Young's modulus and light colors show high values of Young's modulus. The histogram (right) show the statistical distribution. The histogram 4.9b shows the best fit for a bimodal distribution and the histogram 4.9d for a gamma distribution (black line). The red lines represent the three-phase distribution (Li et al., 2018). The normal distributions show separate lines for values between 0 and 25 GPa, 25 and 50 GPa ,and 50 and 100 GPa.

Figure 4.10 shows the results for the spots 3 and 4. The map for spot 3 (Figure 4.10a) shows circles of very low Young's modulus. This could be pore space. The straight horizontal line is caused by an error between trace and retrace curve. The histogram (Figure 4.10a) shows the normal distribution with increased results for the phase from 25 to 50 and from 50 to 100 GPa,
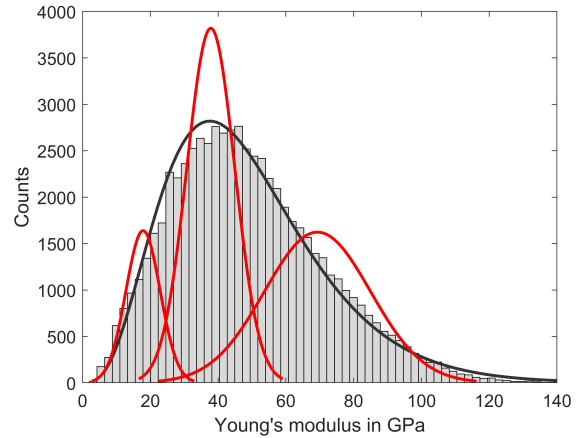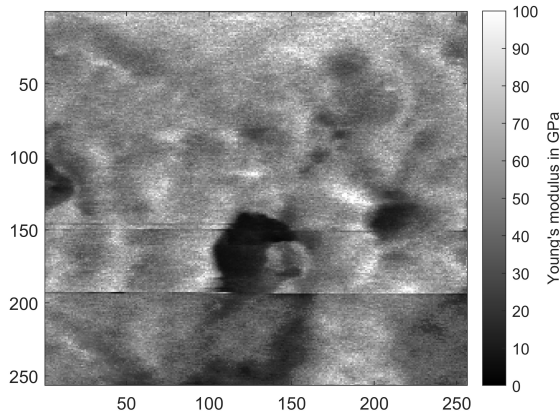
(a) Spot 3 map

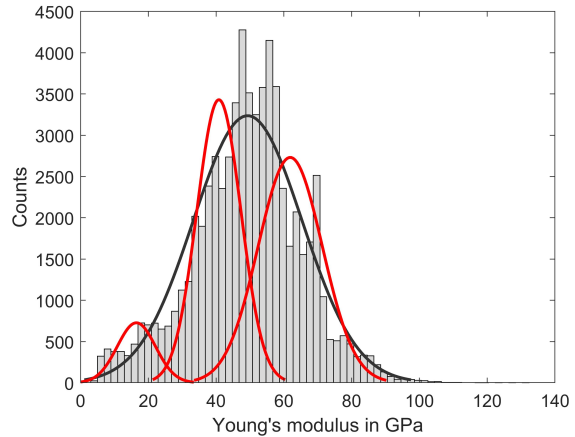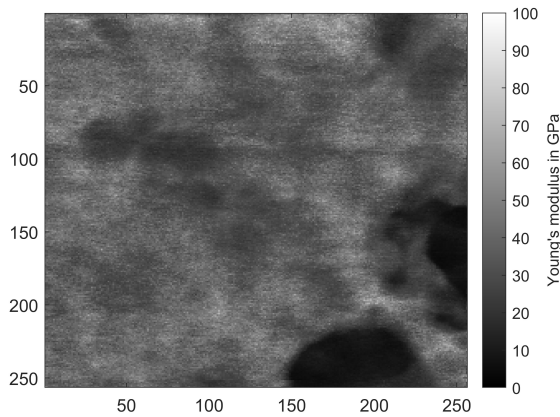(b) Spot 3 histogram

(c) Spot 4 map

(d) Spot 4 histogram

Figure 4.10: Distribution of Young's modulus on a map (left) and a histogram (right). The map on the left shows the 256 x 256 matrix, whereas dark colors indicate low values of Young's modulus and light colors show high values of Young's modulus. The histogram (right) show the statistical distribution. The histogram 4.10b shows the best fit for a normal distribution and histogram 4.10d reveals a bimodal distribution (black line). The red lines represent the three-phase distribution (Li et al., 2018). The normal distributions show separate lines for values between 0 and 25 GPa, 25 and 50 GPa ,and 50 and 100 GPa.

indicating that the majority of the tested material at this spot is of high strength. Spot 4 (Figure 4.10c) shows similar circles of low strength on the edges of the tested spot. The histogram for this spot (Figure 4.10d) shows a bimodal distribution indicating a clear deviation between low values of Young's modulus that could either represent pore space or organic matter and the intermediate phase with higher values of Young's modulus. The histogram, but also the dark colors on the map, show that the overall Young's moduli of this spot show lower values.
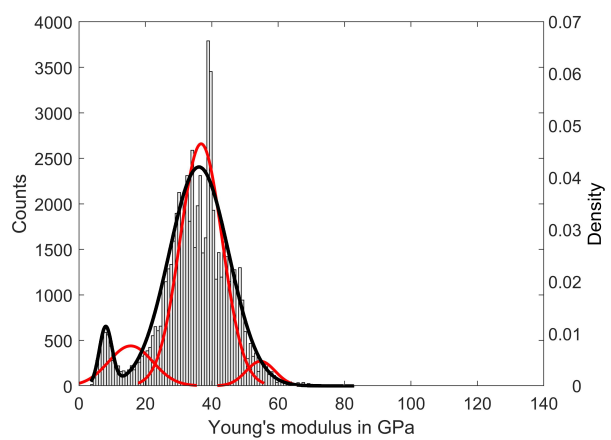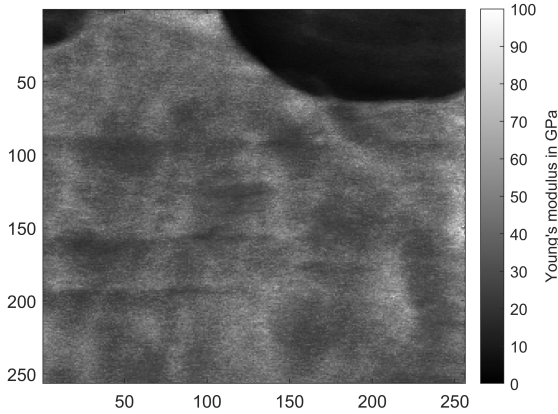
49

(a) Spot 5 map

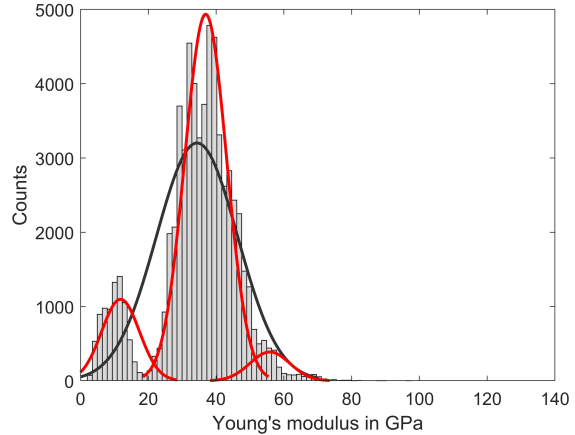(b) Spot 5 histogram
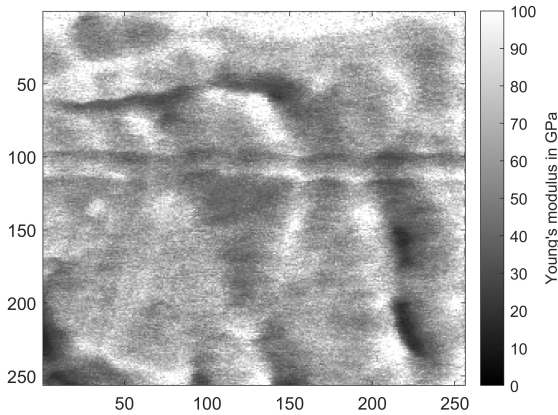
(c) Spot 6 map
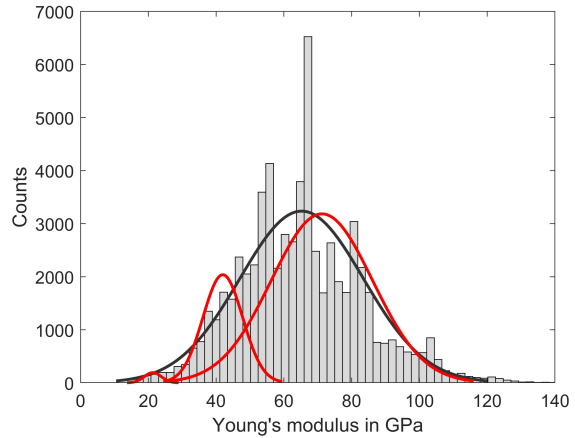
(d) Spot 6 histogram

Figure 4.11: Distribution of Young's modulus on a map (left) and a histogram (right). The map on the left shows the 256 x 256 matrix, whereas dark colors indicate low values of Young's modulus and light colors show high values of Young's modulus. The histogram (right) show the statistical distribution. The histogram 4.11b shows the best fit for a bimodal distribution and histogram 4.11d reveals a normal distribution (black line). The red lines represent the three-phase distribution (Li et al., 2018). The normal distributions show separate lines for values between 0 and 25 GPa, 25 and 50 GPa ,and 50 and 100 GPa.

Figure 4.11 shows the results for the spots 5 and 6. Spot 5 shows a similar distribution of Young's

modulus (Figure 4.11b) as spot 4 (Figure 4.10d). The distribution is bimodal with clear separation

between a phase of approximate Young's modulus 0 to 25 GPa and a phase of 25 to 50 GPa, The

values indicate overall lower value with fewer results or the phase of high strength from 50 to 100

GPa. Spot 6 shows higher values of Young's modulus with small areas of lower Young's modulus,

which could be pore space or nano-fractures. Figure 4.11c shows a horizontal line over the entire

sampling area of this spot. This line is formed during the preparation and does not show the natural topography of the sample. The distribution in the histogram (Figure 4.11d) shows a maximum for higher values of Young's modulus between 50 and 100 GPa.

(a) Spot 7 map

(b) Spot 7 histogram
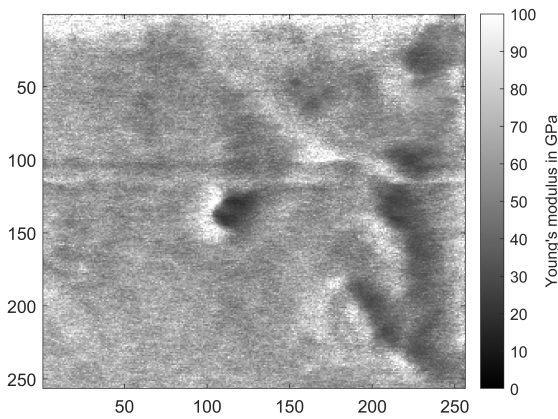
(c) Spot 8 map
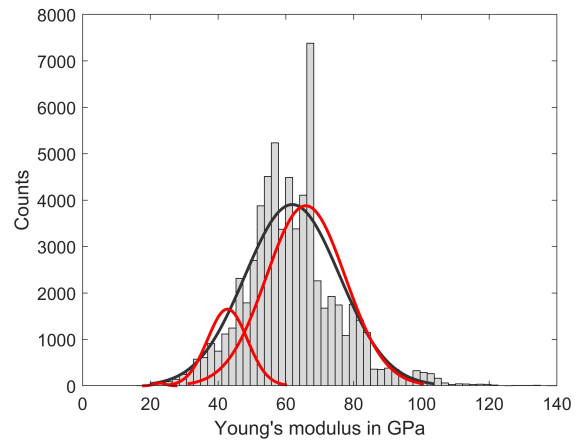
(d) Spot 8 histogram

Figure 4.12: Distribution of Young's modulus on a map (left) and a histogram (right). The map on the left shows the 256 x 256 matrix, whereas dark colors indicate low values of Young's modulus and light colors show high values of Young's modulus. The histogram (right) show the statistical distribution. Histogram 4.12b shows the best fit for a bimodal distribution and histogram 4.12d reveals a normal distribution (black line). The red lines represent the three-phase distribution (Li et al., 2018). The normal distributions show separate lines for values between 0 and 25 GPa, 25 and 50 GPa ,and 50 and 100 GPa.

Figure 4.12 shows the results for the spots 7 and 8. Spot 7 shows a bimodal distribution with a maximum between 0 and 25 GPa for one phase and another maximum between 40 and 60 GPa. The map (Figure 4.12a) shows vertical depressions, which either indicate nano-fractures or organic

matter. Spot 8 shows a tested area of high strength. A phase of low Young's moduli between 0 and 25 GPa does not exits. The lowest values are above 25 GPa. The maximum accumulation in data points is between 50 and 100 GPa.

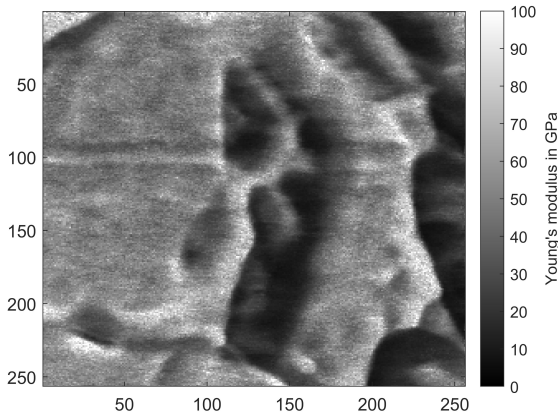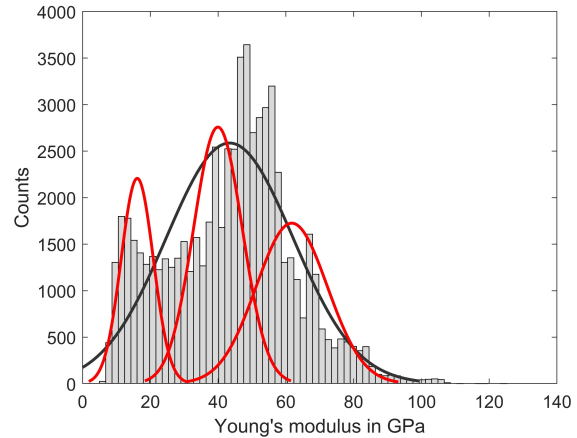(a) Spot 9 map
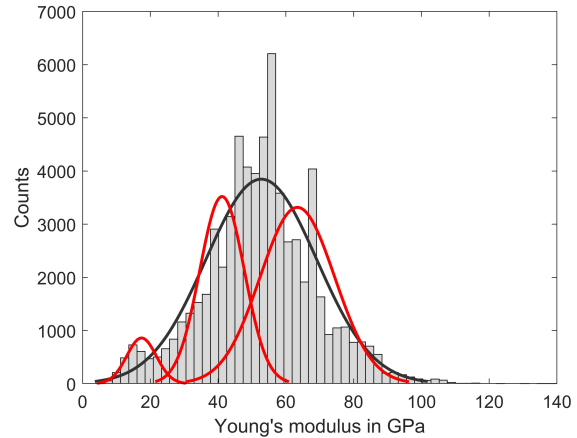
(b) Spot 9 histogram
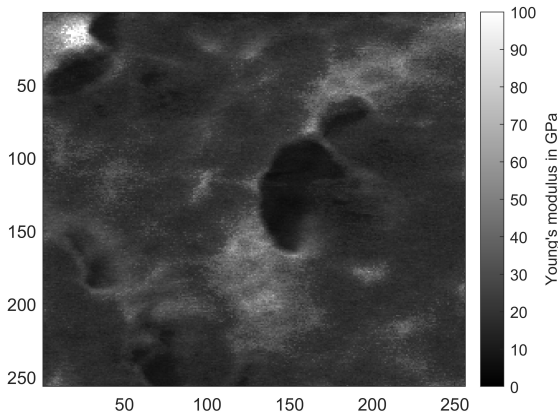
(c) Spot 10 map

(d) Spot 10 histogram

Figure 4.13: Distribution of Young's modulus on a map (left) and a histogram (right). The map on the left shows the 256 x 256 matrix, whereas dark colors indicate low values of Young's modulus and light colors show high values of Young's modulus. The histogram (right) show the statistical distribution. Histogram 4.13b shows the best fit for a normal distribution and 4.13d the best fit for a bimodal distribution (black line). The red lines represent the three-phase distribution (Li et al., 2018). The normal distributions show separate lines for values between 0 and 25 GPa, 25 and 50 GPa ,and 50 and 100 GPa.

Figure 4.13 shows the results for the spots 9 and 10. The map for spot 9 (Figure 4.13a) shows higher values. Along the edges the values increase, indicated by dark spots with an indefinable shape, which could comprise organic matter. A trough indicated by lower values of Young's mod-

ulus follows vertically in 'S'-shape. This could represent a nano-fracture. The horizontal line again, does not represent the topography of the sample and is induced by the preparation. The histogram for spot 9 (Figure 4.13b) is represented by a normal distribution. It shows a small phase with data points from 0 to 25 GPa and many data points for the phases 25 to 50 GPa and 50 to 100 GPa. Overall, the Young's modulus for this spot shows increased values. Opposite of this tested spot is spot 10. The map for spot 10 (Figure 4.13c) shows mostly dark spots. The histogram (Figure 4.13d) shows the maximum peak for the phase from 0 t 25 GPa with a small phase of Young's modulus data for values between 25 and 50 GPa. The phase from 50 to 100 GP does not exist. The low Young's moduli results for this spot indicate the presence of organic matter or pore space.

Figure 4.14 shows the results for the spots 11 and 12. These spots show increased values of Young's modulus indicated by lighter colors on the maps (Figures 4.14a and 4.14c). The histograms for both spots are normally distributed (Figures 4.14b and 4.14d). The phase from 0 t 25 GPa is absent and the phase from 25 to 50 GPa shows only a few data points within this range. For spot 12, the results reach even higher values of Young's modulus than 100 GPa. These spots could represent a quartz or a calcite grain.

Figure 4.15 shows the results for the spots 13 and 14. Spot 13 shows increased values of Young's modulus. The phase from 0 to 25 GPa is absent and there are only few data points for values between 25 and 50 GPa. The maximum in counts is at 70 GPa. The histogram for spot 13 is best represented by a normal distribution (Figure 4.15b). Also, spot 14 shows a normal distribution (Figure 4.15d), but with lower values. All three phases are present, whereas the intermediate phase from 25 to 50 GPa shows most counts. The map for spot 14 (Figure 4.15c) shows dark undefined spots on the bottom left. These spots could indicate organic matter and would explain the phase with values between 0 and 25 GPa.

Figure 4.16 shows the results for the spot 15. The histogram (Figure 4.16b) shows a normal
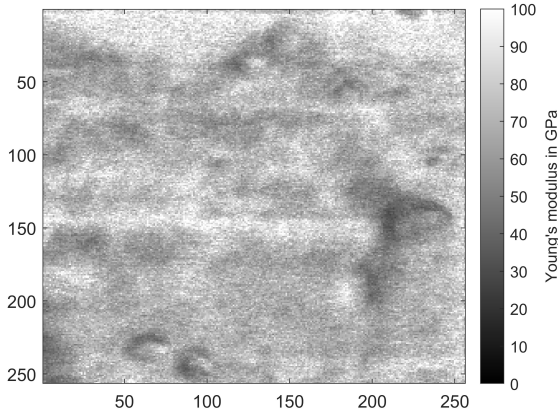
(a) Spot 11 map
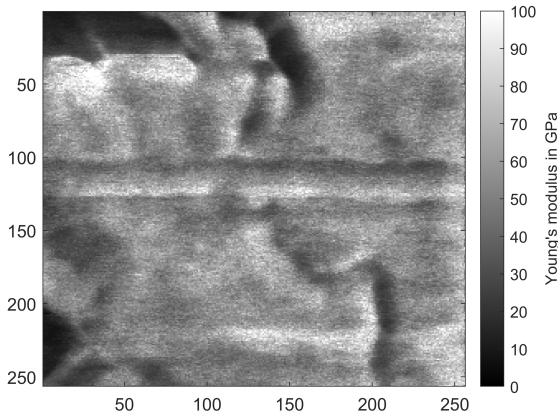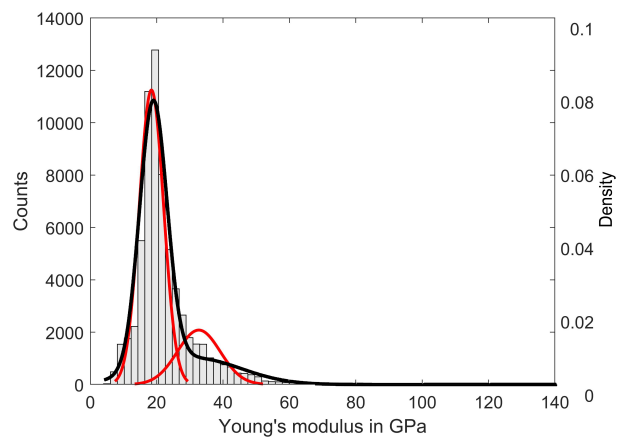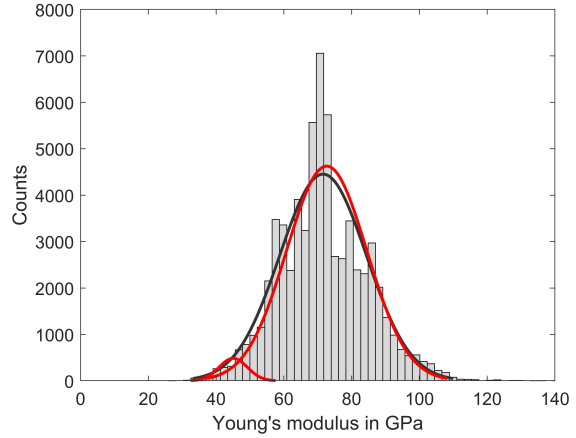
(b) Spot 11 histogram
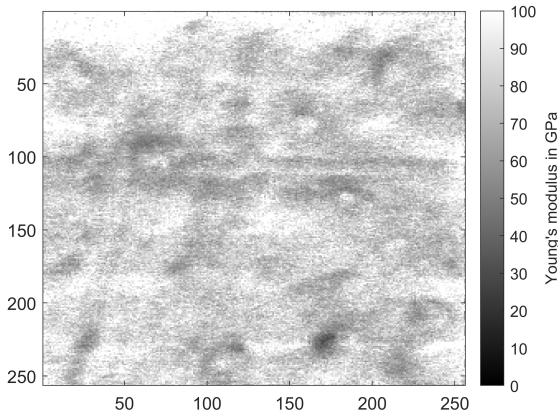
(c) Spot 12 map
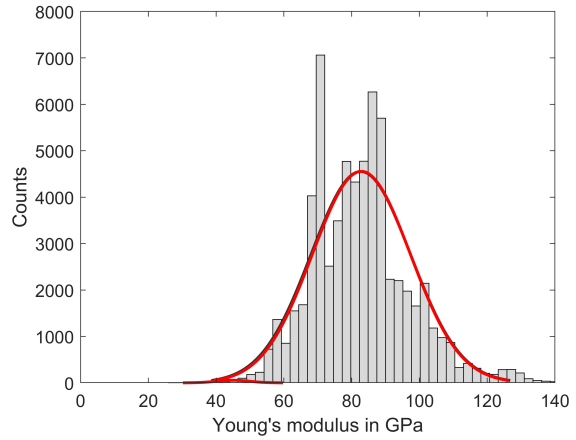
(d) Spot 12 histogram

Figure 4.14: Distribution of Young's modulus on a map (left) and a histogram (right). The map on the left shows the 256 x 256 matrix, whereas dark colors indicate low values of Young's modulus and light colors show high values of Young's modulus. The histogram (right) show the statistical distribution. Histogram 4.14b and 4.14d show the best fit for a normal distribution (black line). The red lines represent the three-phase distribution (Li et al., 2018). The normal distributions show separate lines for values between 0 and 25 GPa, 25 and 50 GPa ,and 50 and 100 GPa.

distribution. The phase from 0 to 25 GPa is nearly absent, whereas the phase with high Young's modulus from 50 to 100 GPa reveals most of the data points. The maximum peak is around 60 GPa. This trend of an increased Young's modulus is confirmed by the graphical interpretation (Figure 4.16a).

The overall distribution of all 15 spots can be seen in figure 4.17a. The mean value for the tested spots is 52.28 GPa with a standard deviation of 21.73 GPa for overall 983,040 counts. A stan-
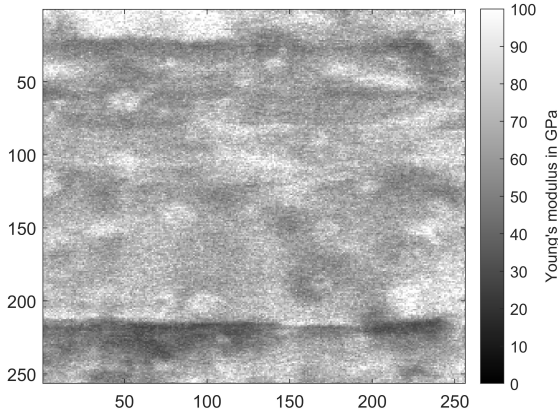
(a) Spot 13 map
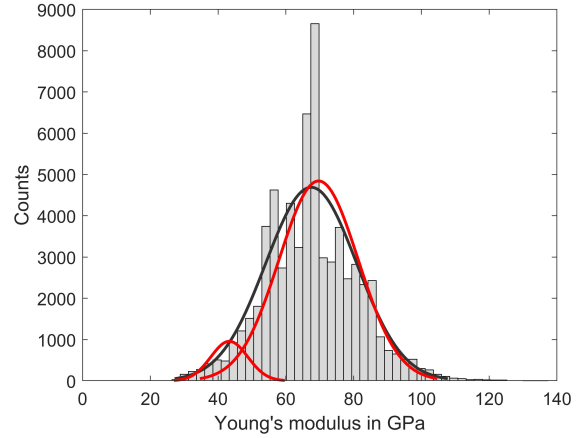
(b) Spot 13 histogram
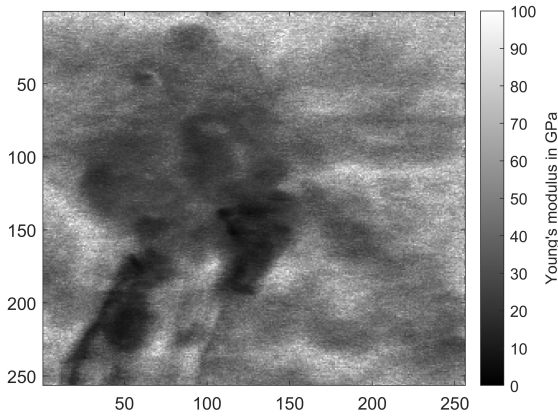
(c) Spot 14 map
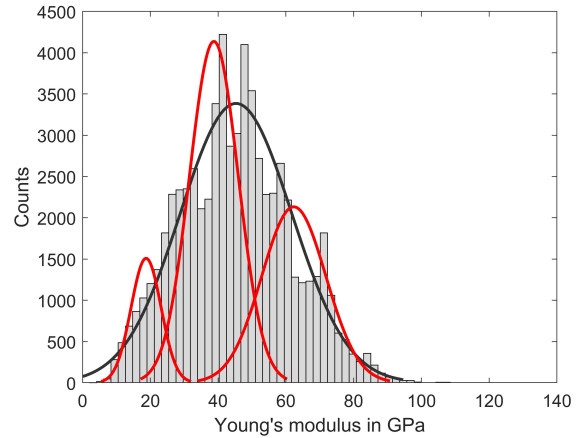
(d) Spot 14 histogram

Figure 4.15: Distribution of Young's modulus on a map (left) and a histogram (right). The map on the left shows the 256 x 256 matrix, whereas dark colors indicate low values of Young's modulus and light colors show high values of Young's modulus. The histogram (right) show the statistical distribution. Histogram 4.15b and 4.15d show the best fit for a normal distribution (black line). The red lines represent the three-phase distribution (Li et al., 2018). The normal distributions show separate lines for values between 0 and 25 GPa, 25 and 50 GPa ,and 50 and 100 GPa.

dard deviation as high as 16 GPa is classified as highly heterogeneous Kumar et al. (2012). This indicates that this sample can be classified as highly heterogeneous. The overall distribution of Poisson's ratio can be seen in figure 4.17b. The preset value of 0.3 has been corrected through the iterative model to a value of 0.2430 with a standard deviation of 0.0620.
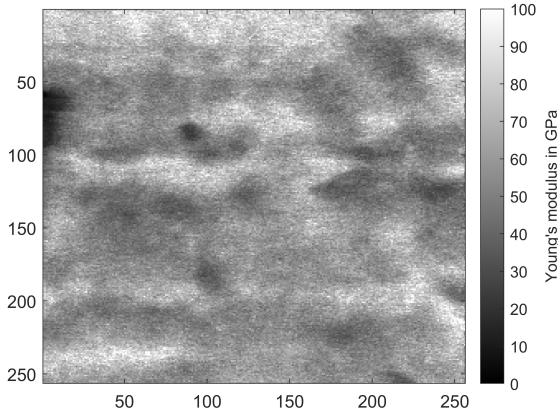
(a) Spot 15 map
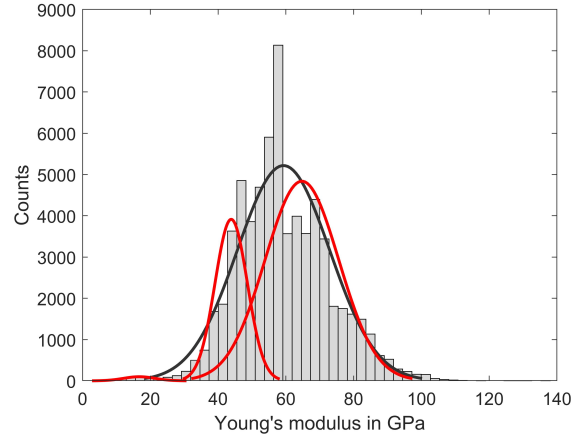
(b) Spot 15 hist

Figure 4.16: Distribution of Young's modulus on a map (left) and a histogram (right). The map on the left shows the 256 x 256 matrix, whereas dark colors indicate low values of Young's modulus and light colors show high values of Young's modulus. The histogram (right) show the statistical distribution. Histogram 4.16b shows the best fit for a normal distribution (black line). The red lines represent the three-phase distribution (Li et al., 2018). The normal distributions show separate lines for values between 0 and 25 GPa, 25 and 50 GPa ,and 50 and 100 GPa.
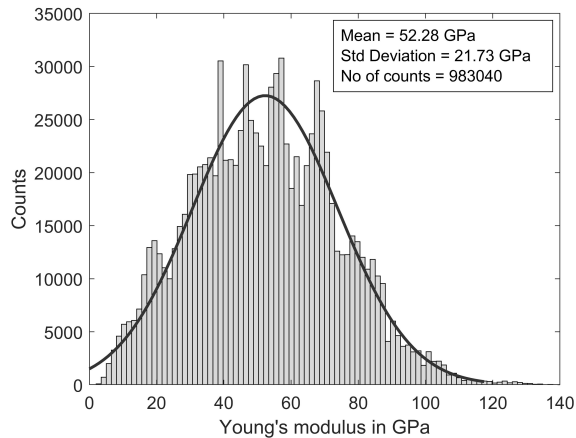
(a) Overall Young's modulus
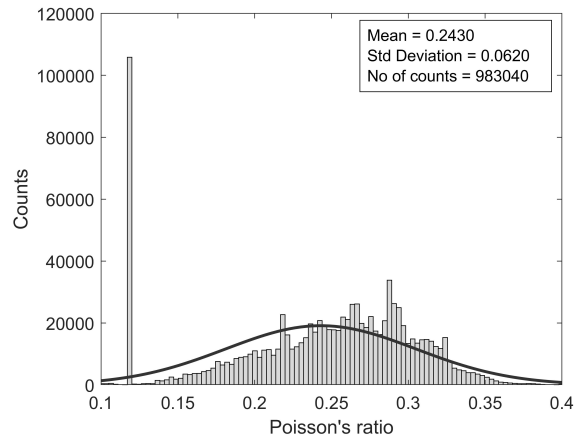
(b) Overall Poisson's ratio

Figure 4.17: Overall distribution of Young's modulus (left) from all 15 spots showing a mean value of 52.28 GPa. The standard deviation is 21.73 GPa for 983040 counts. Overall distribution of Poisson's ratio (right) for from all 15 spots is derived from the iterative model. The original value of 0.3 for every data point has been modified and shows an overall mean value of 0.2430 with a standard deviation of 0.0620. The accumulation in data points for a Poisson's ratio of 0.12 is explained by the minimum of the quadratic fit, which was chosen as best fit for the reference data from figure 4.5. The black lines indicates a normal distribution.

56

4.3.4 Statistical Evaluation

4.3.4.1 Analysis of Variance

The results from the analysis of variance show that the null hypothesis can be rejected (Figure 4.18). The null hypothesis states that the samples are drawn from a population with the same mean. The p-value is less than 0.001 indicating that the groups are not equal, which could be caused by the testing of different components with different material strength.
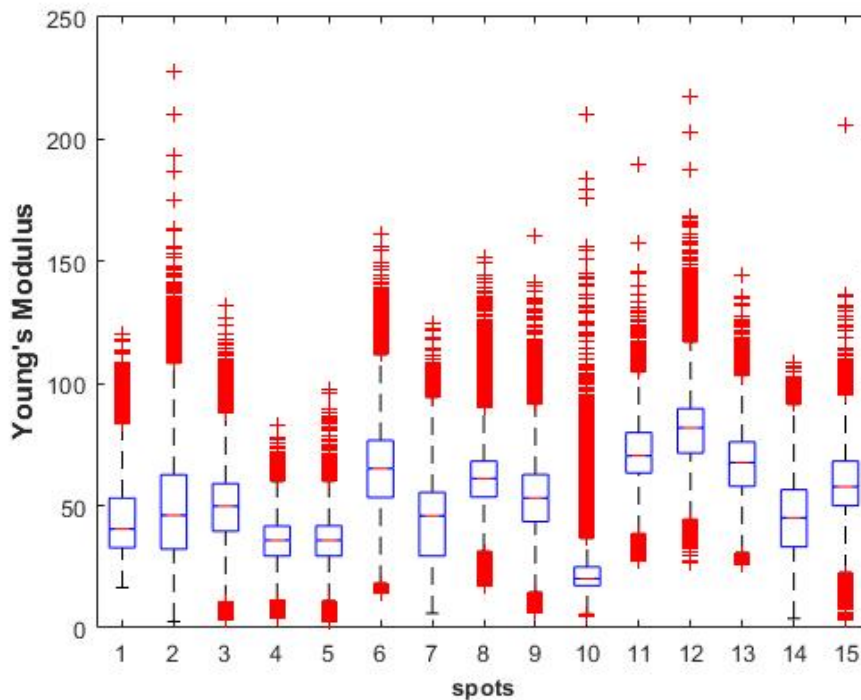
Figure 4.18: Results from analysis of variance for the 15 tested spots revealing that the groups are not equal. The red line within the blue box of each spot indicates the mean value. The red crosses indicate the maximum and the minimum values. The upper and the lower blue line of the box indicate the 75%-ile and the 25%-ile, respectively.

4.3.4.2 Exploratory Factor Analysis

The exploratory factor analysis suggested a 6-factor model, which could explain 34% of the variance in the data set. The model was derived from the scree plot (Figure 4.19) displaying the

eigenvalues. Eigenvalues smaller than 1 are negligible. Values greater than 1 represent significant factors.
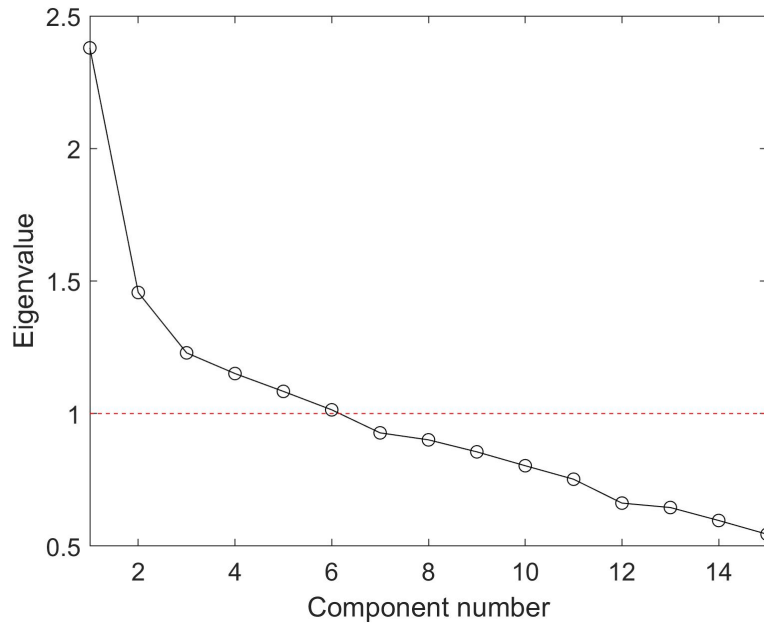
Figure 4.19: Scree plot showing the eigenvalues from the factor analysis and the component numbers. The red dashed line indicates the cut-off values. Values above the red line are significant, values below the dashed line are negligible.

Factor loadings are the correlation coefficients between the observed variables and latent common factors. They are represented in table 4.3. High values indicate strong agreement between a factor and the respective spot. Factor loading smaller than 0.1 indicate poor agreement and are not shown in the table.

Factor 1 shows strong agreement with the spots 3, 4, 6, 8, 11, 12, 13, 14 and 15. Factor 10 shows the strongest agreement with factor 1, but overall still a low factor loading. Most spots that show high factor loading with factor 1 have a high mean value of Young's modulus in common. Therefore, can be assumed that factor 1 represents a group of high strength (for example quartz and calcite minerals). Factor 2 reveals the highest factor loading with spot 5, whereas factor 3 shows the highest factor loading with spot 1. Factor 4 shows a high factor loading with spot 9 and factor 5 indicates strong agreement with spot 3. The mean value of spot 3 is low indicating a weaker

Table 4.3: Factor loadings (regression slopes predicting indicators from latent variables): Higher loadings indicate a greater influence of that latent factor on the measurement outcome for that spot. Factor loadings smaller than 0.1 were excluded from the table. The loading usually range from -1 to 1.

Spots	Factor 1	Factor 2	Factor 3	Factor 4	Factor 5	Factor 6
1			0.959			
2						0.199
3	0.257				0.531	
4	0.283					0.273
5		1.015				
6	0.449			0.141	0.118	
7					0.134	0.524
8	0.451					
9				0.733		
10	0.100					
11	0.435			0.131		
12	0.527					0.103
13	0.270	0.121				
14	0.332				0.164	
15	0.322		0.127			0.101

material strength. Factor 5 also shows an increased factor loading with the spots 6, 7 and 14. This shows that these spots have a weaker material strength in part of the tested raster. Factor 6 shows strong agreement with the spots 2, 4 and 7. These spots show lower values of Young's modulus.

Table 4.4: Uniqueness for each spot.

Spot	1	2	3	4	5	6	7	8
Uniqueness	0.005	0.939	0.611	0.832	0.005	0.749	0.729	0.780

Spot	9	10	11	12	13	14	15	
Uniqueness	0.440	0.796	0.822	0.689	0.924	0.749	0.806	

Table 4.4 shows the Uniqueness for each spot. The uniqueness is the percentage of variance that is not explained by the common factors (Uniqueness=1-communality). It either represents the error or something that is only measured in one variable. If the uniqueness is very high, the communality is low. A high uniqueness and therefore low communality exists for spots that does not show great agreement with the respective factors.

The spots 1, 5 and 9 have a uniqueness smaller than 0.5. These spots show strong agreement with one of the factors, spot 1 with factor 3 (0.959), spot 5 with factor 2 (1.015) and spot 9 with factor 4 (0.733). The spots 2, 3, 4, 6, 7, 8, 10, 11, 12, 13, 14 and 15 have a uniqueness greater than 0.5, whereas spot 2 has the greatest uniqueness close to 1. It shows that these spots yield smaller factor loadings with the factors (table 4.3).

Table 4.5: Correlations between the six different factors.

Spot	Factor 1	Factor 2	Factor 3	Factor 4	Factor 5	Factor 6
Factor 1	1					
Factor 2	-0.0332	1				
Factor 3	0.1989	-0.2723	1			
Factor 4	-0.0483	-0.0895	0.2174	1		
Factor 5	0.1434	-0.1016	0.1054	0.0255	1	
Factor 6	-0.1959	0.1697	0.0189	0.1695	-0.2104	1

Table 4.5 shows the six factors and the correlations to each other. Factor 1 and factor 6 show a poor correlation. Factor one is described as a high strength material, whereas factor 6 has low strength. Factor 5 and factor 6 show a low correlation. Both factors represent weak materials. Possible reason for the poor agreement are different origins of the material's strength. One could represent pore space, whereas the other represents a soft organic phase, both leading to low values of Young's modulus. The poorest agreement is between factor 2 and factor 3 and the strongest agreement between factor 3 and factor 4.

Exploratory factor analysis shows that it is possible to reduce a complex model of a large data set to a smaller set of factors, which represent in this study 34% of the variance of the data set by 6 factors. Factor 1 is expected to be a brittle mineral phase of high strength, possibly resulting from isolated mineral grains. Overall 8 eight spots were found to encompass a stiff inorganic phase, which is explained by the high weight percentages of calcite and quartz. The factors 2, 3 and 4 represent groups of intermediate strength components representing the median intergranular

matrix of the EF formation. Overall, three spots were best explained by an intergranular matrix. Factor 5 and 6 represent a softer rock component such as organic matter and pore space. The mean values of the spots best represented by factor 5 and 6 show a mean Young's modulus higher than 25 GPa. This shows that not only a soft organic phase, but also an intergranular matrix was tested. Overall, four spots are best explained by a soft organic phase or pore space. It is worth to mention, that the groups are overlapping and mostly not only influenced by one factor.

EFA is a powerful statistical method to find similarities between different tested spots and to group the spots based on different tested components. It reveals heterogeneities and therefore improves hydraulic fracturing design by indicating the weakest (spot 10, mean E=21 GPa) and the highest strength (spot 12, mean E=84 GPa) of the tested material.

4.4   True Triaxial Testing

The results from true triaxial testing indicate the anisotropic behavior of the sample and the potential effect of dispersion. Figure 4.20 shows that the Poisson's ratio increases slightly with increasing pressure.

Figure 4.21 shows that p-wave velocity increases strongly between confining stresses of 8 MPa and 15 MPa. This velocity increase for smaller confining stresses is most pronounced in Z-direction. For greater confining stresses, the velocity increases slightly. The greatest velocity is in Y-direction and the smallest in Z-direction. Clear anisotropy of p-wave velocities was observed in X-, Y- and Z-direction. Anisotropy decreases with increasing pressure to minimum of 5% for a confining pressure of 50 MPa.

The s-wave velocities were evaluated in X-, Y- and Z-direction, respectively. When a polarized s-wave enters an anisotropic medium, the shear wave splits into two polarized shear waves. The

61
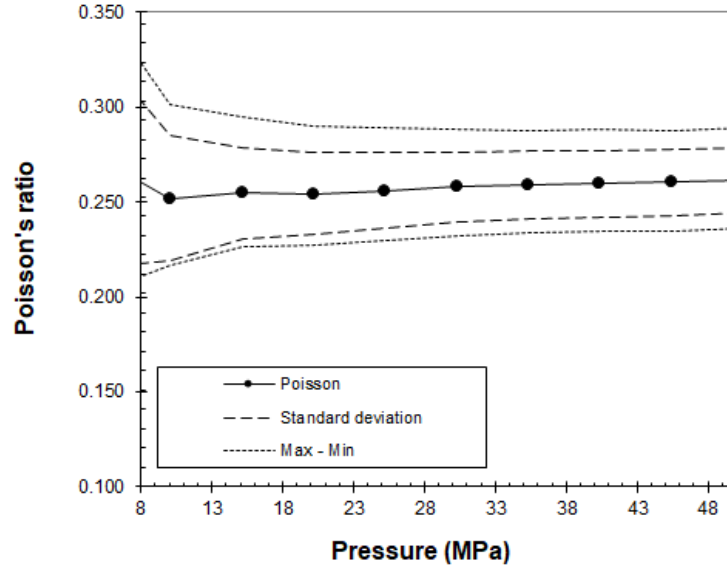
Figure 4.20: Poisson's ratio versus Pressure indicating the Poisson's ratio in solid dots, the standard deviation as dashed line and the maximum and the minimum on the upper and lower boundaries.
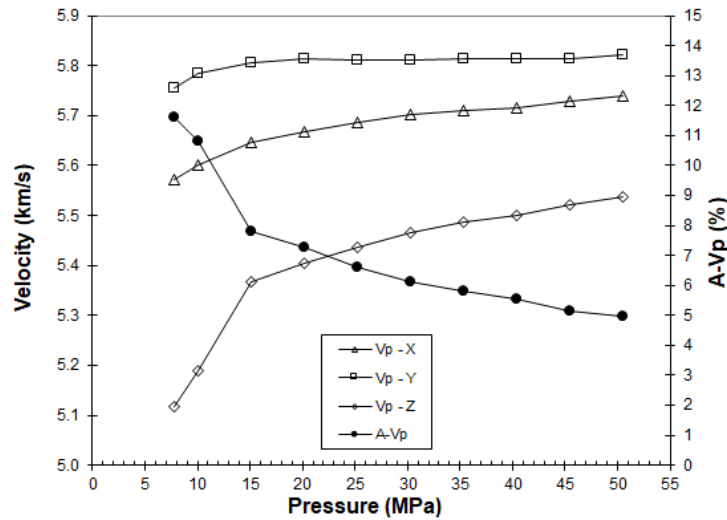
Figure 4.21: Distribution of p-wave velocities with increasing confining pressure in X-, Y- and Z-direction, respectively. The p-wave velocity anisotropy has been calculated for every loading increment.

waves are polarized in YX and ZX in X-direction, in XY and ZY in Y-direction and in XZ and YZ in Z-direction, as the oscillations of the s-wave particles are normal to the direction of wave propagation. Figure 4.22 shows the shear wave splitting in X-direction. It shows that the polarized shear wave in Z-direction is smaller than in Y-direction.
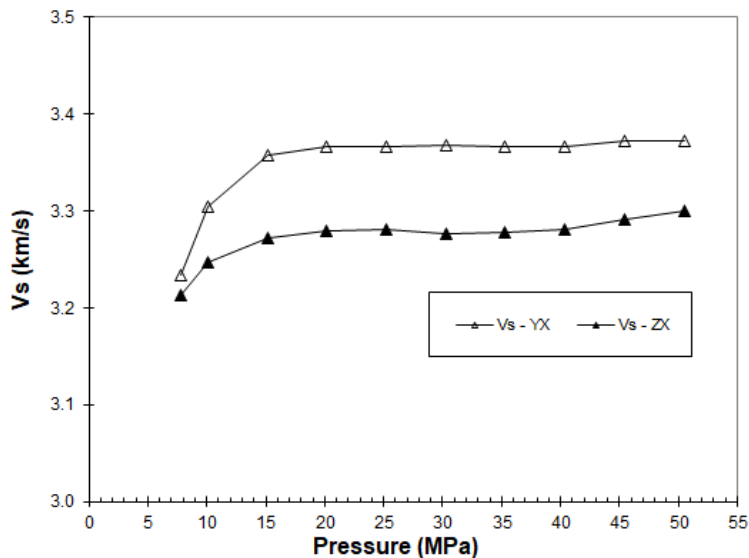
Figure 4.22: S-wave velocity versus Pressure: shear wave splitting in X-direction.

A similar trend can be observed in figure 4.23, indicating lower values for the polarized shear wave in Z-direction.

The polarized shear waves in Z-direction are nearly overlapping in XZ and YZ, as the discrepancies between X- and Y-direction is smaller than in Z-direction. Overall the s-wave velocities reveal the same trend as the p-wave velocities resulting in lower values in Z-direction. It shows that the anisotropic nature of shales leads to different geomechanical properties in X-, Y- and Z-direction. With increasing pressure the elastic properties increase from a Young's modulus of 64.3 GPa at a confining pressure of 8 MPa to a Young's modulus of 69.6 GPa for a confining pressure of 50 MPa. Similar values for the dynamic Young's modulus of 59.25 GPa for the EF formation from true triaxial testing results were found in the literature (Ramezanian and Emadi, 2020).

Heterogeneity leads to different wave velocities in X-, Y- and Z-direction. However, true triaxial testing cannot measure the scale of micro-sized heterogeneity, as it measures the averaged value
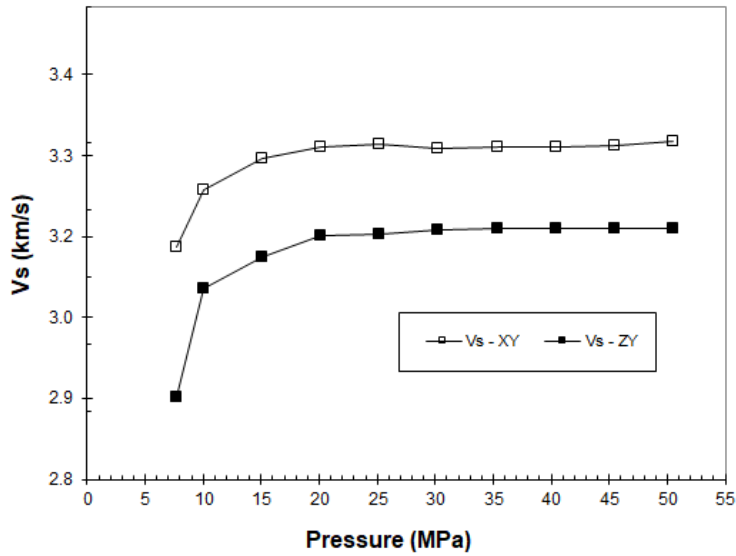
Figure 4.23: S-wave velocity versus Pressure: shear wave splitting in Y-direction.
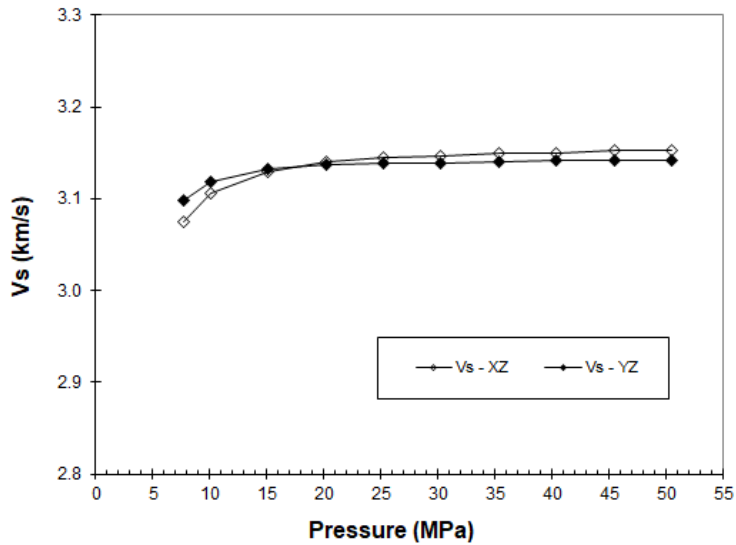
Figure 4.24: S-wave velocity versus Pressure: shear wave splitting in Z-direction.

over the entire 4-cm specimen. Higher values of s-wave velocities in X- and Y-direction can be explained by the foraminifera-rich lamina. Those are filled with calcite and associated with pyrite, which results in higher values of wave velocities and density normal to the stratification (Mokhtari et al., 2014b). Along laminations the tensile strength is lower (Mokhtari et al., 2014a), which

explains the lower velocities in Z-direction additionally. A high calcite content results in a weak anisotropic behavior (Mokhtari et al., 2016) explaining the overlapping the polarized shear waves XZ and YZ in Z-direction.

(a) Effective stress vs. vol. strain

(b) Kstatic/ Kdynamic versus effective stress
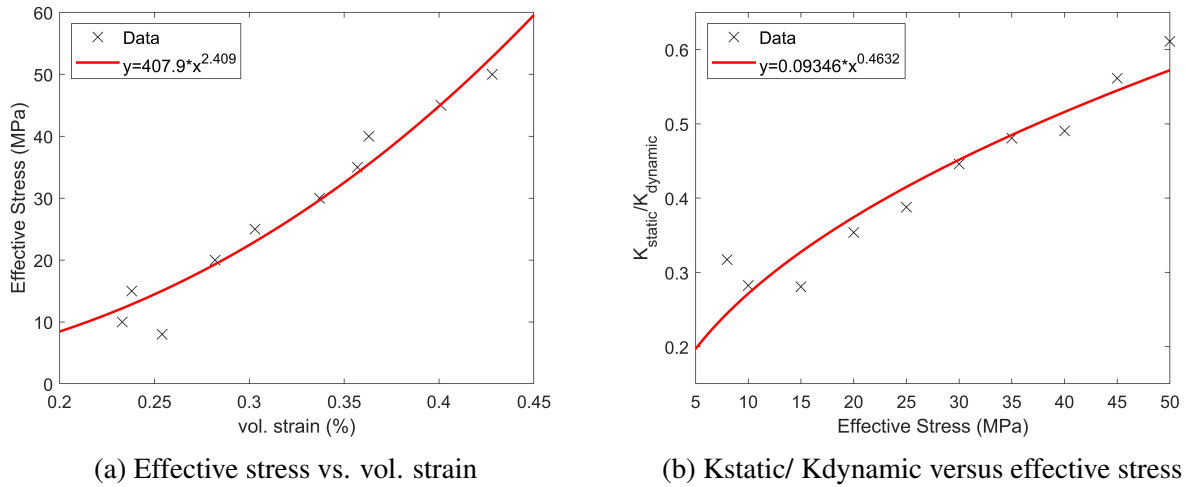
Figure 4.25: Stress strain relationships to derive the static geomechanical properties (left) and the ratio of static to dynamic bulk modulus versus the effective stress (right).

The dynamic Young's modulus for the loading increments 15 MPa to 50 MPa is 69.1 GPa in average, whereas the dynamic bulk modulus is 47.6 GPa. The static bulk modulus is inferred from figure 4.25a (using equation 3.25), which shows the increase in volumetric strain with increasing effective stress. Comparing the static and the dynamic bulk modulus (Figure 4.25b) shows that the dynamic values are significantly higher than the static ones. This divergence between the static and the dynamic modulus has been subject to many studies and has been observed for several rock types (Cheng and Johnston, 1981; Blake and Faulkner, 2016; Holt et al., 2013). It showed that the ratio $K_{static}/K_{dynamic}$ approaches a value of 1 with increasing confining pressure (Blake and Faulkner, 2016). This trend can be confirmed by this work (Figure 4.25b). Empirical correlations that exist to convert dynamic to static values (Mullen et al., 2007) should be handled with care, as it is a strong function of lithology and pressure.

4.5 Connection between AFM PF-QNM and True Triaxial Testing

This study reveals the results for geomechanical testing on three different spacial scales, indicating that different scales of measurements lead to different results.

AFM PF-QNM tests the strength of the material on the smallest scale, which is the tip end radius of 7 nm. It measures the deformation of the material by the cantilever deflection for an applied load. The result indicated the strength of a material to withstand the applied force. It reveals heterogeneities indicating the weakest and the strongest material strength. The testing can be performed on samples that are as small as drill-cuttings. The testing on a sample from the Eagle Ford yield an average static Young's modulus of 52.28 GPa. 15 spots were tested, whereas the weakest spot indicated a Young's modulus of 21 GPa and the strongest of 84 GPa in average.

True triaxial testing measures the seismic velocities of a material for different confining pressures. The dynamic elastic properties are evaluated using Hook's law. The scale for this measurement can be estimated from the velocity frequency relationship:

$$\lambda = \frac{v}{f} = \frac{5700 m/s}{1.5 \times 10^6 Hz} = 3.8 \frac{mm}{cycle} \tag{4.1}$$

where λ is the wavelength, v is the p-wave velocity and f is the frequency of the testing device. It shows that waves with a wave velocity of this rock type are interrogating the material in proportion to the wavelength. It consists of 1.9 mm of compression and 1.9 mm of dilatation parts, respectively. The elastic static and dynamic properties have been evaluate for a confining pressure of 50 MPa. Micro-cracks induced by the drilling process are closed at this confinement, indicated by smaller modulus variations. The dynamic modulus is 69.7 GPa for a confining pressure of 50 MPa.

The static geomechanical properties have been derived from true triaxial testing taking the deformation of the entire sample of the 40 mm cube in account. The static bulk modulus has been

calculated from the stress/strain relationship. The static Young's modulus is 42.6 GPa for a confining pressure of 50 MPa. The static modulus is measured on the largest scale of 40 mm.

The overall evaluation shows that the static Young's modulus is 2/3rd of the dynamic Young's modulus, both derived from true triaxial testing. This is confirmed by measurements on rocks (Cheng and Johnston, 1981; Blake and Faulkner, 2016; Holt et al., 2013) and theoretical work on granular materials (Misra and Nejadsadeghi, 2019). The average result from AFM PF-QNM testing (52.28 GPa) is in between the static (42.6 GPa) an the dynamic (69.7 GPa) triaxial testing results. A likely reason for this divergence AFM PF-QNM and true triaxial testing is that the samples were slightly different in mineralogy, thermal maturity, and diagenetic history. The XRD-analysis revealed that the sample for AFM PF-QNM testing contains about 10% more quartz. Studies on quartz grains indicated an overall higher Young's modulus for quartz than for calcite (Simmons and Wang, 1971). This would lead to overall higher static Young's modulus for the AFM PF-QNM testing, as indicated in this study.

The AFM PF-QNM results, however, are encouraging. The average values are close to the results from true triaxial testing. With further calibration to large-scale tests, AFM PF-QNM could be used on samples that are as small as drill-cuttings in order to provide mechanical constraints for simulations and a 3D-distribution of geomechanical properties to access anisotropy of a material. Using exploratory factor analysis, it is possible to group the results by factors representing a weaker or a phase of high strength.

Chapter 5

Conclusions and Future Work

Abstract

This thesis presents a comparison of geomechanical properties on a nano-scale and on a macro-scale. The chapter encompasses the concluding remarks from AFM PF-QNM testing and from true triaxial testing on samples from the EF formation. Possible and necessary future works are presented.

5.1   Concluding Remarks

This study reveals the potential applicability of AFM PF-QNM testing on small well cuttings instead of large true triaxial testing samples. The following conclusions can be drawn from AFM PF-QNM testing:

- The surface roughness has been evaluated. AFM PF-QNM testing is extremely sensitive to topographical changes and needs extensive preparation using broad beam argon ion milling. The evaluation of the surface roughness ensures that the results are not influences by the surface height. The average surface roughness in this study is 9.4 nm. The statistical evaluation of mean, standard deviation, kurtosis, skewness, minimum height, maximum height and total height are used to evaluate cracks and pore space. Boundary conditions quantifying the quality of the data have been applied.

- An iterative model calculating the Poisson's ratio in dependency of Young's modulus for the EF

formation has been applied. The model is based upon the relationship between Young's modulus and Poisson's ratio derived from experimental studies in the literature. The preset value of 0.3 for Poisson's ratio has been corrected. The new average Poisson's ratio is 0.2430.

- The Young's modulus values vary strongly over the respective tested size of 1 μm^2. Analysis of variance revealed that the group means of the 15 tested spots have no equal mean. This can be interpreted as the testing of different components of the respective spots.

- Exploratory factor analysis was applied to reduce the number of variables to explain the results by a smaller number of factors to explain the result. It was found that 6 factors can explain 34% of the variance. Factor 1 represents a material of high strength, whereas factor 5 and 6 indicate lower values of Young's modulus, which indicate that these factors represent a softer organic phase and pore space. The factors 2, 3 and 4 represent most likely the intergranular matrix. This novel application of EFA for AFM PF-QNM testing allows for 3D mapping of heterogeneities in the sample indicating the location of the weakest and the strongest material components using statistical grouping into phases.

The true triaxial test was employed to measure the elastic properties on a macro-scale. Following conclusions were drawn from true triaxial testing:

- The anisotropic behavior of the EF formation leads to different elastic properties in X-, Y- and Z-directions.

- The seismic wave velocities for p-waves and for s-waves are lower in Z-direction. This could be caused by a low tensile strength along laminations that were found to be foraminifera-rich with calcite and scattered pyrite.

- The seismic velocities increase and the anisotropy decreases with increasing pressure.

- The static Young's modulus is approximately 2/3rd of the dynamic Young's modulus.

The connection between AFM PF-QNM and true triaxial testing reveals, that these tests were performed on different scales. AFM PF-QNM measures the static Young's modulus on a scale of 7 nm, which is the tip end radius. The dynamic Young's modulus is measured on a scale of 3.8 mm/cycle, derived from the velocity frequency relationship. Whereas the static Young's modulus from true triaxial testing is measured on a scale of 40 mm, which is the size of the entire sample. The results indicate that the static Young's modulus is 2/3rd of the dynamic Young's modulus. The static Young's modulus from AFM PF-QNM testing (52.28 GPa) is in between the static (42.6 GPa) and the dynamic (69.7 GPa).

The results show that AFM PF-QNM is potentially a valuable method to derive the geomechanical properties. It reveals mechanical-anisotropy-causing heterogeneities on a nano-scale indicating the weakest and the highest strength. The most pursuing advantage is that it can be performed on samples that are as small as drill-cuttings. It can be applied where the sample material for macro-scale geomechanical testing is non-intact. Further this method can provide a geomechanical log for the horizontal section of the well, which is of paramount value.

5.2   Future Works

The average results from AFM PF-QNM testing show similar values as the results from true triaxial testing. It shows that AFM PF-QNM is worth pursuing. Ultimately a calibration to large-scale mechanical tests should be developed to assess applicability for simulations of hydraulic fracturing. This study shows the application of the iterative model on the EF formation. The model should be expanded to several prolific unconventional reservoirs. Especially, where the lithology is strongly heterogeneous and material extremely brittle and shaly, AFM PF-QNM testing provides an alternative to conventional macro-scale geomechanical testing.

Bibliography

M. Eliyahu, S. Emmanuel, R. J. Day-Stirrat, C. I. Macaulay, Mechanical properties of organic matter in shales mapped at the nanometer scale, Marine and Petroleum Geology 59 (2015) 294–304.

J. Yang, J. Hatcherian, P. C. Hackley, A. E. Pomerantz, Nanoscale geochemical and geomechanical characterization of organic matter in shale, Nature Communications 8 (2017).

Q. Chen, J. Liu, T. Thundat, M. R. Gray, Q. Liu, Spatially resolved organic coating on clay minerals in bitumen froth revealed by atomic force microscopy adhesion mapping, Fuel 191 (2017) 283–289.

C. Li, M. Ostadhassan, S. Guo, T. Gentzis, L. Kong, Application of PeakForce tapping mode of atomic force microscope to characterize nanomechanical properties of organic matter of the Bakken Shale, Fuel 233 (2018) 894–910.

S. L. Eichmann, D. Jacobi, M. H. Haque, N. A. Burnham, NON-DESTRUCTIVE INVESTIGATIONS OF THE THERMAL MATURITY AND MECHANICAL PROPERTIES OF SOURCE ROCKS, Journal of Petroleum Geology 41 (2018) 421–446.

C. Li, M. Ostadhassan, T. Gentzis, L. Kong, H. Carvajal-Ortiz, B. Bubach, Nanomechanical characterization of organic matter in the Bakken formation by microscopy-based method, Marine and Petroleum Geology 96 (2018) 128–138.

W. V. Grieser, J. M. Bray, Identification of Production Potential in Unconventional Reservoirs, SPE Production and Operations Symposium (2007).

D. M. Jarvie, R. J. Hill, T. E. Ruble, R. M. Pollastro, Unconventional shale-gas systems: The Mississippian Barnett Shale of north-central Texas as one model for thermogenic shale-gas assessment, AAPG Bulletin 91 (2007) 475–499.

R. Rickman, M. J. Mullen, J. E. Petre, W. V. Grieser, D. Kundert, A Practical Use of Shale Petrophysics for Stimulation Design Optimization: All Shale Plays Are Not Clones of the Barnett Shale, SPE Annual Technical Conference and Exhibition (2008) 1–11.

F. P. Wang, J. F. Gale, Screening Criteria for Shale-Gas Systems, Gulf Coast Association of Geological Societies Transactions 59 (2009) 779–793.

D. Buller, S. Hughes, J. Market, E. Petre, D. Spain, T. Odumosu, Petrophysical Evaluation for Enhancing Hydraulic Stimulation in Horizontal Shale Gas Wells, SPE Annual Technical Conference and Exhibition (2010) 22–32.

J. C. Glorioso, A. J. Rattia, Unconventional Reservoirs: Basic Petrophysical Concepts for Shale Gas, SPE/EAGE European Unconventional Resources Conference and Exhibition (2012) 20–22.

R. K. Sharma, S. Chopra, New attribute for determination of lithology and brittleness, Society of Exploration Geophysicists (2012) 1–7.

S. Z. Sun, K. N. Wang, P. Yang, S. Key, Integrated Prediction of Shale Oil Reservoir Using Pre-Stack Algorithms for Brittleness and Fracture Detection, International Petroleum Technology Conference (2013).

J. Chen, G. Zhang, H. Chen, X. Yin, The construction of shale rock physics effective model and prediction of rock brittleness The construction of shale rock physics effective model and prediction of rock brittleness, SEG Denver 2014 Annual Meeting (2014) 2861–2865.

X. Jin, S. N. Shah, J.-C. Roegiers, B. Zhang, An Integrated Petrophysics and Geomechanics Approach, SPE Hydraulic Fracturing Technology Conference (2014) 4–6.

A. Alzahabi, G. Alqahtani, M. Y. Soliman, R. M. Bateman, G. Asquith, R. Vadapalli, Fracturability Index is a Mineralogical Index: A new approach for fracturing decision, Society of Petroleum Engineers 2 (2015) 178033.

E. Rybacki, A. Reinicke, T. Meier, M. Makasi, G. Dresen, What controls the mechanical properties of shale rocks ? – Part I : Strength and Young ' s modulus, Journal of Petroleum Science and Engineering 135 (2015) 702–722.

K. S. Mews, M. M. Alhubail, R. G. Barati, A review of brittleness index correlations for unconventional tight and ultra-tight reservoirs, 2019. doi:10.3390/geosciences9070319.

I. R. Kivi, M. Ameri, H. Molladavoodi, Shale brittleness evaluation based on energy balance analysis of stress-strain curves, Journal of Petroleum Science and Engineering 167 (2018) 1–19.

T. Cook, J. Perrin, V. Wagener, Hydraulically fractured horizontal wells account for most new oil and natural gas wells, 2018. URL: https://www.eia.gov/todayinenergy/detail.php?id=34732.

E. Geary, U.S. crude oil production grew 17% in 2018, surpassing the previous record in 1970, 2019. URL: https://www.eia.gov/todayinenergy/detail.php?id=38992.

A. Ghanizadeh, C. R. Clarkson, S. Aquino, O. H. Ardakani, H. Sanei, Petrophysical and geomechanical characteristics of Canadian tight oil and liquid rich gas reservoirs: II. Geomechanical property estimation, Fuel 153 (2015) 682–691.

A. Mazaheri, H. Memarian, B. Tokhmechi, B. N. Araabi, Developing fracture measure as an index of fracture impact on well-logs, Energy Exploration and Exploitation 33 (2015) 555–574.

L. Bond, K. Denslow, J. Griffin, G. Dale, R. Harris, T. Moran, D. Sheen, T. Schenkel, Evaluation of non-nuclear techniques for well logging: Technology evaluation, US Department of Energy 35 (2010) 493–500.

P. Poorsolhjouy, A. Misra, Effect of intermediate principal stress and loading-path on failure of cementitious materials using granular micromechanics, International Journal of Solids and Structures 108 (2017) 139–152.

W. Li, A. Sakhaee-Pour, Macroscale Young's Moduli of Shale Based on Nanoindentations, PETROPHYSICS 597 PETROPHYSICS 57 (2016) 597–603.

K. Liu, M. Ostadhassan, H. Jabbari, B. Bubach, Potential Application of Atomic Force Microscopy in Characterization of Nano-pore Structures of Bakken Formation, Society of Petroleum Engineers (2016) 5–6.

G. Simmons, H. Wang, Single Crystals Elastic Constants and Calculated Aggregate Properties, Cambridge, Mass., M.I.T. Press, 1971.

T. M. Wilkinson, S. Zargari, M. Prasad, C. E. Packard, Optimizing nano-dynamic mechanical analysis for high-resolution, elastic modulus mapping in organic-rich shales, Journal of Materials Science 50 (2015) 1041–1049.

P. Shukla, Nanoindentation Studies on Shales, Ph.D. thesis, University of Oklahoma, 2013.

D. Hu, L. Matzar, V. Martysevich, Effect of Natural Fractures on Eagle Ford Shale Mechanical Properties, Society of Petroleum Engineers (2014).

Z. Ye, A. Ghassemi, S. Riley, Stimulation Mechanisms in Unconventional Reservoirs, SPE/AAPG/SEG Unconventional Resources Technology Conference 2018, URTC 2018 (2018).

M. Mokhtari, M. M. Honarpour, A. N. Tutuncu, G. N. Boitnott, Characterization of elastic anisotropy in Eagle Ford shale: Impact of heterogeneity and measurement scale, SPE Reservoir Evaluation and Engineering 19 (2016) 429–439.

O. Akrad, J. Miskimins, M. Prasad, The Effects of Fracturing Fluids on Shale Rock Mechanical Properties and Proppant Embedment, Society of Petroleum Engineers (2011).

P. Shukla, V. Kumar, M. Curtis, C. H. Sondergeld, C. S. Rai, Nanoindentation Studies on Shales, American Rock Mechanics Association (2013).

P. Shukla, S. Taneja, C. Sondergeld, C. Rai, Nanoindentation Measurements on Rocks, Conference Proceedings of the Society for Experimental Mechanics Series. Springer, Cham 5 (2014) 99–105.

H. Corapcioglu, . J. L. Miskimins, M. Prasad, SPE-170835-MS Fracturing Fluid Effects on Young's Modulus and Embedment in the Niobrara Formation, Society of Petroleum Engineers (2014) 27–29.

A. N. Flotron, E. K. Franseen, R. H. Goldstein, Sedimentologic and stratigraphic controls on reservoir sweet spots in the Wolfcamp 'A,' Howard County, Midland Basin, SPE/AAPG/SEG Unconventional Resources Technology Conference 2019, URTC 2019 (2019).

P. C. Hackley, T. Zhang, A. M. Jubb, B. J. Valentine, F. T. Dulong, J. J. Hatcherian, Organic petrography of Leonardian (Wolfcamp A) mudrocks and carbonates, Midland Basin, Texas: The fate of oil-prone sedimentary organic matter in the oil window, Marine and Petroleum Geology 112 (2020).

I. Gupta, C. Rai, C. Sondergeld, D. Devegowda, Rock Typing in Wolfcamp Formation, Society of Petrophysicists and Well Log Analysts (2017).

V. Kumar, C. H. Sondergeld, C. S. Rai, Nano to Macro Mechanical Characterization of Shale, Society of Petroleum Engineers (2012).

W. Pu, EOS Modeling and Reservoir Simulation Study of Bakken Gas Injection Improved Oil Recovery in the Elm Coulee Field, Montana, Ph.D. thesis, Colorado School of Mines, 2013.

Y. Cho, E. Eker, I. Uzun, X. Yin, H. Kazemi, Rock Characterization in Unconventional Reservoirs: A Comparative Study of Bakken, Eagle Ford, and Niobrara Formations, Society of Petroleum Engineers (2016).

H. Li, Effects of Water Content, Mineralogy, and Anisotropy on the Mechanical Properties of Shale Gas Rocks, Ph.D. thesis, University of Louisianna at Lafayette, 2017.

T. A. Jansen, The Effect of Rock Properties n Hydraulic Fracture Conductivity in the Eagle Ford and Fayetteville Shales, Ph.D. thesis, Texas A&M University, 2014.

S. M. Ergene, Lithologic heterogeneity of the Eagle Ford Formation, South Texas, Thesis (2014) 202.

Y. Wang, D. H. Han, S. Aldin, M. Aldin, X. Qin, Static and dynamic Young's moduli and Poisson's ratios of Eagle Ford shale under triaxial tests, 2018 SEG International Exposition and Annual Meeting, SEG 2018 (2018) 3613–3617.

M. Mokhtari, B. Thanh Bui, A. N. Tutuncu, Tensile Failure of Shales: Impacts of Layering and Natural Fractures, Society of Petroleum Engineers (2014a).

M. Mokhtari, M. M. Honarpour, A. N. Tutuncu, G. N. Boitnott, SPE-170707-MS Acoustical and Geomechanical Characterization of Eagle Ford Shale-Anisotropy, Heterogeneity and Measurement Scale, Society of Petroleum Engineers (2014b) 27–29.

X. Jin, S. Shah, J.-C. Roegiers, A Practical Petrophysical Approach for Brittleness Prediction from Porosity and Sonic Logging in Shale Reservoirs, Society of Petroleum Engineers (2014).

R. Kohli, K. L. Mittal, Development in Surface Contamination and Cleaning, William Andrew, 2012. doi:10.1016/C2009-0-64376-2.

H. Hertz, Ueber die Berührung fester elastischer Körper, Journal für die reine und angewandte Mathermatik (1881) 156–171.

J. N. Israelachvili, Contrasts between Intermolecular, Interparticle, and Intersurface Forces, in: Intermolecular and Surface Forces, Elsevier, 2011, pp. 205–222. doi:10.1016/b978-0-12-375182-9.10011-9.

B. V. Derjaguin, V. M. Muller, Y. P. Toporov, Effect of Contact Deformations on the Adhesion of Particles, Journal of Colloid and Interface Science 53 (1975) 314–326.

V. Kumar, M. E. Curtis, N. Gupta, C. H. Sondergeld, C. S. Rai, Estimation of Elastic Properties of Organic Matter and Woodford Shale Through Nano-indentation Measurements, Society of Petroleum Engineers (2012).

Bruker-Corporation, Document Revision History: PeakForce QNM User Guide User Guide, 2011.

K. C. Bennett, L. A. Berla, W. D. Nix, R. I. Borja, Instrumented nanoindentation and 3D mechanistic modeling of a shale at multiple scales, Acta Geotechnica 10 (2015).

M. Cała, K. Cyran, M. Kawa, M. Kolano, D. Łydzba, M. Pachnicz, M. Rajczakowska, A. Rózański, M. Sobótka, D. Stefaniuk, A. Stopkowicz, D. Wałach, Identification of Microstructural Properties of Shale by Combined Use of X-Ray Micro-CT and Nanoindentation Tests, in: Procedia Engineering, volume 191, Elsevier Ltd, 2017, pp. 735–743. doi:10.1016/j.proeng.2017.05.239.

Y. Zhang, M. Lebedev, A. Al-Yaseri, H. Yu, X. Xu, M. Sarmadivaleh, A. Barifcani, S. Iglauer, Nanoscale rock mechanical property changes in heterogeneous coal after water adsorption, Fuel 218 (2018) 23–32.

P. Trtik, J. Kaufmann, U. Volz, On the use of peak-force tapping atomic force microscopy for quantification of the local elastic modulus in hardened cement paste, Cement and Concrete Research 42 (2012) 215–221.

Y. Liu, Fracture Toughness Assessment of Shales by Nanoindentation, Ph.D. thesis, University of Massachusetts Amherst, 2015. URL: https://doi.org/10.7275/jzym-1g18. doi:10.7275/jzym-1g18.

I. Gupta, C. Sondergeld, C. Rai, Applications of NanoIndentation for Reservoir Characterization in Shales, American Rock Mechanics Association (2018).

K. Liu, M. Ostadhassan, B. Bubach, Application of nanoindentation to characterize creep behavior of oil shales, Journal of Petroleum Science and Engineering 167 (2018) 729–736.

S. Mighani, S. Taneja, C. H. Sondergeld, C. S. Rai, Nanoindentation Creep Measurements on Shale, American Rock Mechanics Association (2015).

S. Zhao, Y. Li, Y. Wang, Z. Ma, X. Huang, Quantitative study on coal and shale pore structure and surface roughness based on atomic force microscopy and image processing, Fuel 244 (2019) 78–90.

Y. Li, J. Yang, Z. Pan, W. Tong, Nanoscale pore structure and mechanical property analysis of coal: An insight combining AFM and SEM images, Fuel 260 (2020).

S. Huang, A. Misra, Path-dependent analysis of elastic sphere contact subjected to tangential loading with varying directions, Proceedings of the Institution of Mechanical Engineers, Part J: Journal of Engineering Tribology 226 (2012) 678–686.

T. W. Lambe, R. V. Whitman, Soil Mechanics, Massachusetts Institute of Technology: John Liley & Sons, 1969.

W. W. Dickinson, S. S. Aravind, S. R. Higgins, S. Berg, B. M. Suijkerbuijk, H. C. Schniepp, Using atomic force spectroscopy to study oil/mineral interactions at reservoir temperatures and pressures, Fuel 259 (2020).

H. Gercek, Poisson's ratio values for rocks, 2007. doi:10.1016/j.ijrmms.2006.04.011.

O. Enriquez-Tenorio, A. Knorr, D. Zhu, A. D. Hill, Relationships Between Mechanical Properties and Fracturing Conductivity for the Eagle Ford Shale, SPE Production & Operations 34 (2019) 318–331.

J. M. Andrade, S. Muniategui, P. Lbpez-Mahia, D. Prada, Use of multivariate techniques in quality control of kerosene production, Fuel 76 (1997) 51–59.

V. Jain, C. Minh, N. Heaton, P. Ferraris, L. Ortenzi, S. Mauro, T. Ribeiro, CHARACTERIZA-
TION OF UNDERLYING PORE AND FLUID STRUCTURE USING FACTOR ANALYSIS
ON NMR DATA, Society of Petrophysicists and Well Log Analysts (2013).

R. Maskey, J. Fei, H. O. Nguyen, Use of exploratory factor analysis in maritime research, Asian
Journal of Shipping and Logistics 34 (2018) 91–111.

T. Brown, Confirmatory factor analysis for applied research, 2015.

S. E. Kim, I. W. Seo, S. Y. Choi, Assessment of water quality variation of a monitoring network
using exploratory factor analysis and empirical orthogonal function, Environmental Modelling
and Software 94 (2017) 21–35.

L. R. Fabrigar, D. T. Wegener, Exploratory Factor Analysis, Oxford University Press, Incorporated,
2012.

H. B. Motra, F. Wuttke, Temperature dependence of elastic - and s-wave properties of rocks:
applications to geothrmal reservoir evaluation, Kiel: Energy Geotechnics - 1st international
conference on energy geotechnics, ICEGT (2016).

N. Riazi, C. R. Clarkson, A. Ghanizadeh, A. Vahedian, S. Aquino, J. M. Wood, Determination
of elastic properties of tight rocks from ultrasonic measurements: Examples from the Montney
Formation (Alberta, Canada), Fuel 196 (2017) 442–457.

G. Mavko, T. Mukerji, J. Dvorkin, The Rock Physics Handbook, 2009.

O. O. Blake, D. R. Faulkner, The effect of fracture density and stress state on the static and
dynamic bulk moduli of Westerly granite, Journal of Geophysical Research: Solid Earth 121
(2016) 2382–2399.

H. B. Motra, H. H. Stutz, Geomechanical Rock Properties Using Pressure and Temperature De-
pendence of Elastic P- and S-Wave Velocities, Geotechnical and Geological Engineering 36
(2018) 3751–3766.

O. Enriquez-Tenorio, A COMPREHENSIVE STUDY OF THE EAGLE FORD SHALE FRAC-TURE CONDUCTIVITY, Ph.D. thesis, Texas A&M University, 2016.

O. Enriquez-Tenorio, A. Knorr, D. Zhu, A. D. Hill, Relationships between mechanical properties and fracturing conductivity for the eagle ford shale, Society of Petroleum Engineers - SPE Asia Pacific Hydraulic Fracturing Conference (2016) 318–331.

J. Liu, X. Jiang, X. Huang, S. Wu, Morphological characterization of super fine pulverized coal particle. Part 2. AFM investigation of single coal particle, Fuel 89 (2010) 3884–3891.

M. Ramezanian, H. Emadi, Investigating effects of temperature and confining pressure on dynamic elastic properties and permeability—An experimental study, Geomechanics for Energy and the Environment 22 (2020).

C. H. Cheng, D. H. Johnston, DYNAMIC AND STATIC MODULI, GEOPHYSICAL RE-SEARCH LETTERS 8 (1981) 39–42.

R. M. Holt, E. Fjaer, A. Bauer, Static and Dynamic Moduli - so equal, and yet so different, American rock mechanics association (2013).

M. Mullen, R. Roundtree, B. Barree, A Composite Determination of Mechanical Rock Properties for Stimulation Design (What to do When You Don't Have a Sonic Log), Society of Petroleum Engineers (2007).

A. Misra, N. Nejadsadeghi, Longitudinal and transverse elastic waves in 1D granular materials modeled as micromorphic continua, Wave Motion 90 (2019) 175–195.